

Article

Long-Term Variability of Relationships between Potential Large-Scale Drivers and Summer Precipitation in North China in the CERA-20C Reanalysis

Lan Dai  and Jonathon S. Wright * 

Department of Earth System Science, Tsinghua University, Beijing 100084, China; dail15@mails.tsinghua.edu.cn
* Correspondence: jswright@tsinghua.edu.cn

Abstract: Although much progress has been made in identifying the large-scale drivers of recent summer precipitation variability in North China, the evolution of these drivers over longer time scales remains unclear. We investigate multidecadal and interannual variability in North China summer precipitation in the 110-year Coupled ECMWF Reanalysis of the Twentieth Century (CERA-20C), considering changes in regional moisture and surface energy budgets along with nine circulation indices linked to anomalous precipitation in this region. The CERA-20C record is separated into three distinct periods according to the running climatology of summer precipitation: 1901–1944 (neutral), 1945–1979 (wet), and 1980–2010 (dry). CERA-20C reproduces expected relationships between large-scale drivers and regional summer precipitation anomalies well during 1980–2010, but these relationships generally do not extend to earlier periods. For example, a strong relationship with the Eurasian teleconnection pattern only emerges in the late 1970s, while correlations with the El Niño–Southern Oscillation and the Pacific–Japan pattern change sign in the mid-twentieth century. We evaluate two possible reasons for this nonstationarity: (1) the underlying atmospheric model may require strong data assimilation constraints to capture large-scale circulation influences on North China, or (2) large-scale drivers inferred from recent records may be less general than expected. Our analysis indicates that both factors contribute to the identified nonstationarity in CERA-20C, with implications for the reliability of seasonal forecasts and climate projections based on current models.

Keywords: precipitation; North China; teleconnection; centennial-scale reanalysis



Citation: Dai, L.; Wright, J.S. Long-Term Variability of Relationships between Potential Large-Scale Drivers and Summer Precipitation in North China in the CERA-20C Reanalysis. *Atmosphere* **2021**, *12*, 81. <https://doi.org/10.3390/atmos12010081>

Received: 9 December 2020

Accepted: 3 January 2021

Published: 7 January 2021

Publisher's Note: MDPI stays neutral with regard to jurisdictional claims in published maps and institutional affiliations.



Copyright: © 2021 by the authors. Licensee MDPI, Basel, Switzerland. This article is an open access article distributed under the terms and conditions of the Creative Commons Attribution (CC BY) license (<https://creativecommons.org/licenses/by/4.0/>).

1. Introduction

Located along the northern edge of the East Asian summer monsoon (EASM), North China frequently experiences hydrological dry and wet extremes arising from anomalous EASM circulation patterns [1]. Rainfall associated with the EASM in July and August accounts for roughly two-thirds of the total annual precipitation in North China [2–4]. Large variations in summer rainfall make this region vulnerable to meteorological disasters, such as droughts and rainstorms. North China has experienced frequent summer droughts and extreme precipitation events in recent decades, which caused immense damages to agricultural productivity, ecosystem health, and human lives and livelihoods [5–9].

A number of studies have documented variability in summer precipitation over North China at interannual to multidecadal time scales [1,10]. In particular, a significant decadal shift to drier conditions has been identified in the late 1970s, in comparison to relatively wet conditions during the 1950s to mid-1960s [1]. Summer drought events have occurred relatively frequently in North China since the late 1970s, owing to a weakened EASM and the associated “North Drought–South Flood” pattern [11,12]. The decadal shift toward a weaker EASM around the end of the 1970s has been variously attributed to a phase shift of the Pacific decadal oscillation (PDO) from negative to positive [13,14], upper-

tropospheric cooling over mid-latitude East Asia [15,16], global warming [17], and aerosol forcing [18,19].

Interannual variability of summer precipitation in North China has been linked to variations in regional circulation systems, including the EASM, the western Pacific subtropical high (WPSH), and the East Asian westerly jet (EAWJ) [2,20–22]. Empirical evidence indicates that summer precipitation anomalies are positively correlated with the strength of the EASM and the latitudinal location of the WPSH [2,5], while the seasonal evolution of the EASM rain belt is dynamically controlled by the northward migration of the upper-level EAWJ [21,22]. A southward displacement of the EAWJ is associated with weaker southwesterly winds and decreased precipitation in North China, with the opposite anomalies observed when the EAWJ is located farther north than normal [10,23].

Tropical and extratropical conditions both play important roles in forcing the aforementioned regional circulation anomalies. Among tropical factors, the El Niño–Southern Oscillation (ENSO) ranks as a leading-order forcing of interannual variability in summer precipitation over North China [6,24]. Summer precipitation deficits in North China are generally observed during summers when El Niño is developing, in contrast to precipitation increases during summers when El Niño is decaying. However, statistical links between ENSO variability and summer precipitation in North China are unstable in time and do not consistently reach standard thresholds for statistical significance [25,26]. Hypotheses explaining ENSO influences on summer precipitation in North China have generally centered around two teleconnection patterns. First, the Pacific–Japan (PJ) teleconnection pattern is initiated by anomalous convective activity over the western tropical Pacific under the influence of ENSO-related sea surface temperature (SST) anomalies [27–29]. Second, anomalous diabatic heating in the South Asian summer monsoon region during ENSO transitions modulates the circumglobal teleconnection (CGT) pattern along the subtropical westerly jet [30], which has in turn been linked to precipitation anomalies in North China [31–33]. Recent studies have also argued that extratropical circulation patterns, such as the Eurasian (EU) teleconnection pattern forced by anomalies in Arctic sea ice cover and/or Eurasian snow cover, exert significant influences on summer precipitation in North China [5,6,33]. The North Atlantic Oscillation has been linked to variations in the EU pattern during boreal summer [34].

A number of studies have evaluated relationships between large-scale circulation patterns and anomalous summer precipitation in North China during recent decades [5,6,32,33]. However, the potential changes in relationships between these large-scale factors (e.g., PJ, CGT, and EU) and summer precipitation in North China over longer time scales are not well understood. Long-term historical reanalysis products are valuable tools for examining how relationships between potential large-scale forcings and regional-scale responses may vary on decadal to centennial scales [35,36]. Although these extended reanalysis products are subject to large uncertainties, they must nonetheless maintain consistency with both assimilated observations and the internal dynamics of the model system used to conduct the reanalysis. In the context of this study, the assimilated observations (mainly comprising SST, surface pressure, and ocean surface winds) provide valuable constraints on large-scale circulation patterns, while the atmospheric model plays a key role in determining how those large-scale patterns relate to regional precipitation anomalies in North China. The data assimilation systems used to conduct century-scale reanalyses also often share common frameworks with those used to conduct weather forecasts, climate projections, and full-input reanalyses that focus on recent decades. Assessments based on extended historical reanalyses thus serve two key purposes. First, they provide a unique test of hypotheses developed based on data for recent decades: Does the full reanalysis record support the hypothesis? Do deviations from the hypothesis appear to arise mainly from actual variations in the climate system or from intrinsic limitations of the reanalysis framework? Second, they provide important validation of the underlying model and data assimilation systems: Are relationships identified for recent decades preserved when

upper-atmospheric constraints are removed? How well does the system perform in the early part of the record when all observational constraints are sparse?

Here, we assess the long-term variability of relationships between potential large-scale drivers and summer precipitation anomalies in North China during 1901–2010 based on outputs from the Coupled ECMWF Ocean–Atmosphere Reanalysis of the Twentieth Century (CERA-20C). We also evaluate the performance of the CERA-20C reanalysis in terms of long-term variability in summer precipitation over North China and associated large-scale circulation indices. The paper is organized as follows. The data and methods used in the study are introduced in Section 2. In Section 3, long-term variability in summer precipitation over North China and relevant large-scale circulation patterns are described. In Section 4, possible limitations of the CERA-20C data are discussed, along with their implications for the results. Our conclusions are then summarized in Section 5.

2. Data and Methods

2.1. Data

CERA-20C is a climate reanalysis of the twentieth century produced by ECMWF's coupled ocean–atmosphere assimilation system that assimilates surface pressure, ocean surface winds, and ocean temperature and salinity measurements [37]. The output data cover the period 1901–2010 at a default horizontal resolution of $1.125^\circ \times 1.125^\circ$. CERA-20C provides ten ensemble members to better account for errors in the forecast model and uncertainties in the observational data assimilation. The ensemble spread in CERA-20C gradually decreases over time, indicating increased confidence in the reanalysis state as the quantity and quality of assimilated observations improve. Monthly surface and vertically-integrated variables used in this study include precipitation; surface radiation, sensible, and latent heat fluxes; total column water vapor; surface pressure; and sea surface temperature. Monthly specific humidities, geopotential heights, zonal and meridional winds, and vertical pressure velocities on 23 pressure levels between 1000 hPa and 200 hPa are also used.

CERA-20C precipitation products are evaluated against two centennial-scale gauge-based reconstructions of monthly precipitation over land that cover the period 1901–2010: (1) the Climatic Research Unit (CRU) Timeseries (V4.0) precipitation analysis [38,39]; and (2) the gridded monthly precipitation dataset (V3.01) produced by the University of Delaware (UDEL) [40]. Both reconstructions are provided on a $0.5^\circ \times 0.5^\circ$ horizontal grid.

2.2. Moisture Budget Equation

A regional moisture budget is diagnosed to provide context for the causes of interannual variability in summer precipitation. The moisture budget is conducted on pressure coordinates [41]:

$$P' - E' = -\langle u\partial_x q \rangle' - \langle v\partial_y q \rangle' - \langle \omega\partial_p q \rangle' + \delta', \quad (1)$$

where P is precipitation, E is evaporation, q is specific humidity, p is pressure, u , v , and ω are the zonal, meridional and vertical (pressure) wind velocities, respectively, and δ represents the budget residual. The prime denotes a departure from the climatology. $\langle \rangle$ represents the density-weighted vertical integration from the monthly-mean surface pressure (p_s) to an upper bound near the tropopause (p_t). The pressure of the upper bound is set to 200 hPa for this analysis. Monthly mean fields are used to diagnose the moisture budget terms.

2.3. Climate Indices

The following climate indices are used in this study following hypotheses put forward in the literature:

- (1) The PDO index is defined as the leading empirical orthogonal function (EOF) of monthly SST anomalies over the North Pacific Ocean poleward of 20° N after removing both the climatological annual cycle and global mean SST anomaly [42].

- (2) The Niño 3.4 index is calculated as the average SST anomaly within the region 5° N–5° S, 120° W–170° W.
- (3) The PJ pattern is defined as the leading EOF of relative vorticity at 850 hPa within the domain 0° N–45° N, 100° E–160° E [43].
- (4) The CGT pattern is defined as the leading EOF of meridional wind at 200 hPa within the domain 20° N–60° N, 0° E–150° E [31].
- (5) The EU pattern index is defined as the linear combination of area mean geopotential heights in three anomaly centers at 500 hPa (A1: 60° N–70° N, 55° E–85° E; A2: 40° N–55° N, 90° E–110° E; A3: 30° N–40° N, 110° E–130° E; $EUI = -Z'_{A1} + 2Z'_{A2} - Z'_{A3}$) [33].
- (6) The meridional displacement of the EAWJ is defined as the difference in area-mean zonal wind at 200-hPa between 45° N–55° N, 100° E–140° E and 32.5° N–42.5° N, 100° E–140° E [23].
- (7) The EASM index is defined as the area mean horizontal wind velocity at 850 hPa within the domain 30° N–40° N, 115° E–125° E [5].
- (8) The WPSH is defined as the area mean geopotential height at 850 hPa over the domain 15° N–30° N, 120° E–150° E [44].
- (9) The upper-tropospheric temperature (UTT) is represented by the difference of area mean geopotential height between 200 hPa and 500 hPa over North China domain (32° N–42° N, 105° E–120° E) [45].

All indices (including Niño 3.4) are calculated separately for each ensemble member based on monthly-mean fields at $1.125^\circ \times 1.125^\circ$ resolution. For the PJ and CGT indices, the principal components during 1901–2010 are derived by projecting anomaly fields from CERA-20C onto the leading EOFs identified for 1979–2017 using the atmosphere-only ERA5 reanalysis [33,46]. This step ensures that the PJ and CGT indices calculated for CERA-20C are spatially consistent with circulation patterns evaluated in previous work. Index-based representations of large-scale circulation patterns can only crudely represent the complexity of variations in the large-scale circulation. However, the use of climate indices adopted from previous studies allow us to more clearly link our results to the context provided by those studies.

Anomalies in indices and other evaluated variables are calculated by subtracting the mean annual cycle based on a 30-year running climatology. The climatology is held constant for the first 15 years and last 15 years of the record to enable analysis of the full 1901–2010 period. The use of a running climatology helps to separate multidecadal variability (including spurious drifts in the reanalysis state) from interannual variability, allowing us to analyze each time scale in turn. Pearson correlations are calculated between the large-scale climate indices and summer precipitation anomalies in North China.

3. Results

3.1. Long-Term Climatology and Interannual Variability of Summer Precipitation

We first evaluate the summer (July–August) precipitation climatology in CERA-20C against the CRU and UDEL gauge-based analyses. Figure 1 shows regionally averaged summer precipitation over North China (32° N–42° N, 105° E–120° E) during the period 1901–2010. Running 30-year climatologies of summer precipitation based on the CERA-20C ensemble mean, CRU, and UDEL are shown in the upper portion of Figure 1a as dashed lines. The 30-year running climatology from the CERA-20C ensemble mean, which takes values ranging from 4.07 mm d^{-1} to 5.04 mm d^{-1} , is consistently larger than those from CRU (3.82 mm d^{-1} to 4.19 mm d^{-1}) or UDEL (3.86 mm d^{-1} to 4.28 mm d^{-1}). This positive bias indicates that the CERA-20C reanalysis overestimates summer precipitation in North China relative to observations. However, the bias in CERA-20C gradually reduces over time as more observations become available for assimilation. Significant decadal shifts from wet to dry conditions around the late 1970s are evident in both the CERA-20C reanalysis and the observational time series. This shift toward reduced summer precipitation in North China is consistent with previous results reporting a weakening of the EASM in the late 1970s [1,15,17].

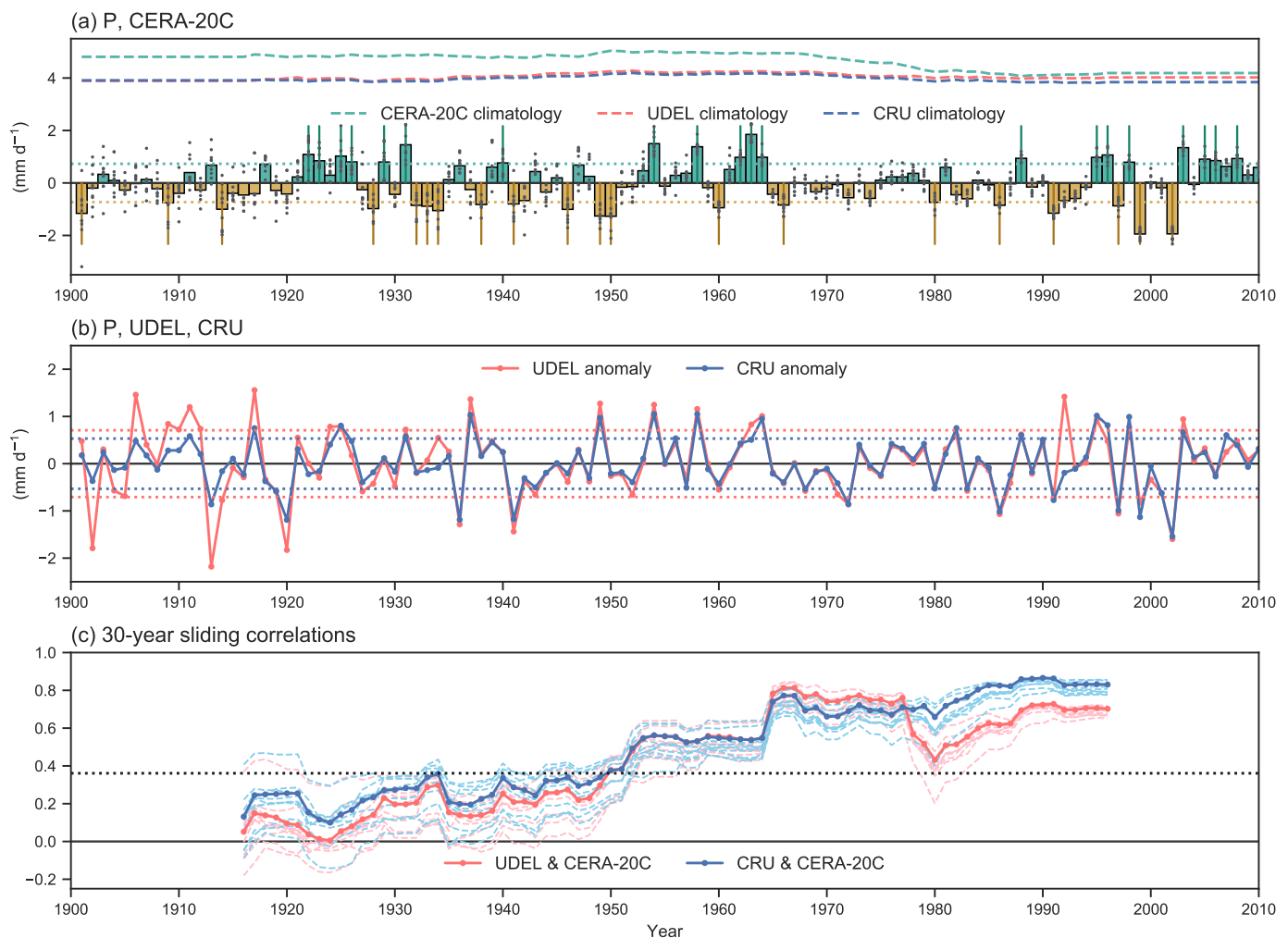


Figure 1. (a) Time series of area-mean July–August precipitation anomalies over North China based on the Coupled ECMWF Ocean–Atmosphere Reanalysis of the Twentieth Century (CERA-20C) ensemble (bars: ensemble mean; dots: individual ensemble members) relative to the 30-year running climatology (green dashed line). The driest and wettest years are marked with brown and green vertical lines, respectively; dotted horizontal lines indicate the $\pm 1\sigma$ standard deviation (σ) thresholds used to identify these years. (b) Time series of precipitation anomalies from University of Delaware (UDEL) (red line) and Climatic Research Unit (CRU) (blue line). The respective 30-year running climatologies are shown in (a) for ease of comparison with CERA-20C. Dotted horizontal lines indicate $\pm 1\sigma$ for each dataset. (c) Thirty-year sliding correlations of precipitation anomalies from the CERA-20C ensemble mean (heavy lines) and individual members (light lines) against those based on UDEL (red) and CRU (blue) during 1901–2010. The black dotted line represents the 95% confidence level for 30-year correlations based on Student's *t* test.

The late-1970s decrease in CERA-20C is sharper than that in CRU or UDEL, so that the CERA-20C climatology is in good agreement with the gauge-based analyses after the early 1980s. The most obvious candidate for explaining this reduced regional precipitation bias is improvements in the quality and quantity of assimilated observations. However, it is important to emphasize that observations assimilated in CERA-20C are limited to surface pressure, ocean surface winds, and ocean temperature and salinity measurements [37]. None of these assimilated variables provides direct constraints on the vertical structure or moisture content of the atmosphere. Accordingly, data assimilation-driven improvement in precipitation must emerge through changes in the circulation that alter in turn the horizontal distribution of moisture source regions, the vertical distribution of moisture transport, cloud fields and associated surface flux responses, or other features of the atmospheric water cycle (see Section 3.2).

Summer precipitation anomalies based on the ten CERA-20C ensemble members and the ensemble mean are shown in the lower part of Figure 1a. The CERA-20C ensemble mean precipitation anomalies show strong interannual variability with a standard deviation of 0.73 mm d^{-1} . This value corresponds to around 15–18% of the July–August mean, in good agreement with estimates for recent decades based on other data sets [33]. The standard deviation in CERA-20C is larger than that based on CRU (0.53 mm d^{-1} ; 12–13%) but comparable to that based on UDEL (0.71 mm d^{-1} ; 17–18%). Forty extremely dry and wet years (relative to the 30-year running climatology) are selected based on the criterion that the CERA-20C ensemble mean anomaly exceeds one standard deviation. The twenty extremely dry years include 1901, 1909, 1914, 1928, 1932, 1933, 1934, 1938, 1941, 1946, 1949, 1950, 1960, 1966, 1980, 1986, 1991, 1997, 1999, and 2002 (brown vertical lines in Figure 1a). The twenty extremely wet years include 1922, 1923, 1925, 1926, 1929, 1931, 1940, 1954, 1958, 1962, 1963, 1964, 1988, 1995, 1996, 1998, 2003, 2005, 2006, and 2008 (green vertical lines in Figure 1a). Two periods of relatively weak variability stand out in the CERA-20C ensemble mean time series: before 1920 and from the mid-1960s through the late 1970s. The weak ensemble mean anomalies in first two decades of the twentieth century contrast with relatively large anomalies in individual members, as large spread causes substantial cancellation within the ensemble. The spread among the ten ensemble members then reduces over time, with tighter clusters in recent years relative to the early part of the record. Accordingly, small ensemble mean anomalies from the mid-1960s through the late 1970s reflect consistently weak departures from the climatology in all individual members rather than cancellation of opposing anomalies within the ensemble.

Observation-based time series of precipitation anomalies from CRU and UDEL are presented in Figure 1b. The two time series of observed summer precipitation anomalies are largely consistent since the mid-1930s, but show large uncertainty and low confidence in the magnitude of precipitation anomalies at the beginning of the twentieth century. Figure 1c shows 30-year sliding correlations of precipitation anomalies in the CERA-20C ensemble relative to those based on UDEL (pink lines) and CRU (blue lines). Correlations between precipitation anomalies from CERA-20C and those from the two observational analyses do not consistently exceed 0.4 until around 1950. However, the correlations increase substantially after that year, often reaching values around 0.8 after 1965. Biases in both the reanalysis relative to the observations and the observations relative to each other have reduced over time, especially after the late 1970s, as the observing system has expanded and improved.

Spatial patterns of the July–August precipitation climatology and anomalies for wet and dry years are shown for three distinct periods in Figure 2. Based on analysis of the 30-year running climatology (Figure 1a), we divide the full CERA-20C period (1901–2010) into three parts: 1901–1944 (early/neutral), 1945–1979 (middle/wet), and 1980–2010 (late/dry). The climatologies for 1945–1979 (Figure 2b) and 1980–2010 (Figure 2c) are shown as differences relative to the mean distribution for 1901–1944 (Figure 2a) to better illustrate the scale and regional context of multi-decadal changes in the CERA-20C precipitation climatology. Figure 2b shows that mean precipitation increased slightly during 1945–1979 relative to the early period over most parts of North China (marked by the red box). By contrast, the precipitation pattern during 1980–2010 (Figure 2c) reveals substantial decreases in North and Northeast China relative to the early period, along with increases over the Yangtze River Valley, South Korea, and southern Japan. The composite mean precipitation anomalies for wet and dry years with anomalies larger than ± 1 standard deviation during each time period are shown in Figure 2d–i. Composite patterns for wet and dry years are more symmetric and more isolated within North China in the early part of the record relative to the later part. The canonical “North Drought–South Flood” pattern is well captured for composite dry years during 1980–2010 (Figure 2i). However, this pattern is not evident for dry years based on CERA-20C during 1901–1944 or 1945–1979, and the dipole pattern for composite wet years during 1980–2010 is rotated toward a more southeast-to-northwest axis.

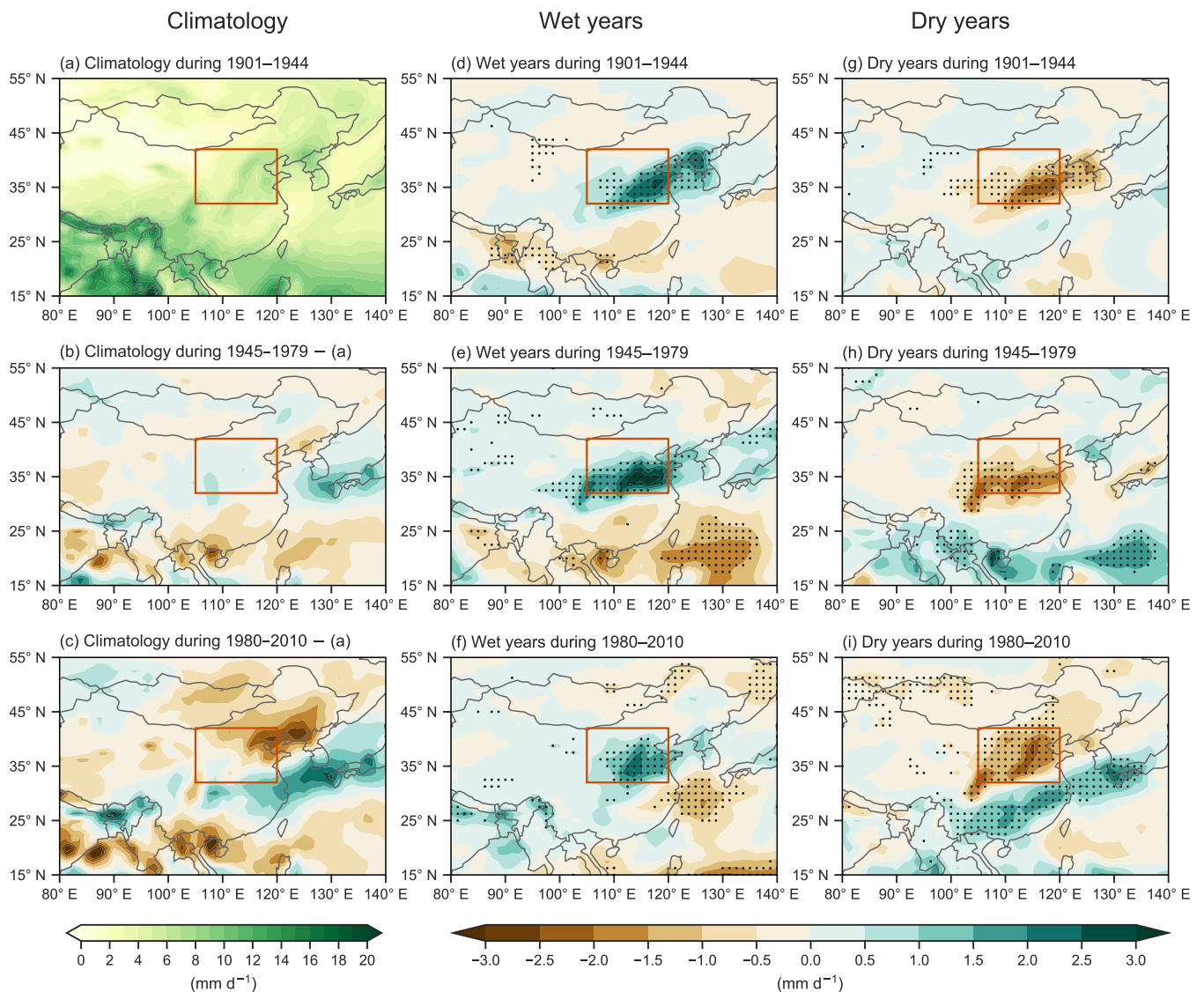


Figure 2. Spatial patterns of (a–c) July–August precipitation climatology, (d–f) composite July–August precipitation anomalies for twenty wet years, and (e–i) composite July–August precipitation anomalies for twenty dry years during three different periods: (a,d,g) 1901–1944, (b,e,h) 1945–1979, and (c,f,i) 1980–2010 based on the CERA-20C ensemble mean. Climatologies in (b,c) are shown as differences relative to (a). Stippling in (d–i) indicates that anomalies are statistically significant at the 95% confidence level.

3.2. Long-Term Variations in Moisture and Energy Budgets

3.2.1. Atmospheric Moisture Budget

Interannual anomalies in component terms of the moisture budget can provide insight into the underlying causes of long-term variability in summer precipitation in the CERA-20C reanalysis. Time series of July–August anomalies in area-averaged total column water vapor over North China during 1901–2010 are shown in Figure 3a for the ensemble mean and each ensemble member. The 30-year running climatology of total column water vapor shows a pronounced decrease of roughly 10% (about 4 kg m^{-2}) over the 30 years between 1950 and 1980. This decrease in total column water vapor may have contributed to the relatively dry conditions in North China since the late 1970s, particularly as represented in CERA-20C (Figure 1a). July–August anomalies of total column water vapor exhibit strong interannual variability since at least the 1930s, though weak variability in the ensemble mean for the early twentieth century is again partly due to inconsistent signs

of anomalies among the ten CERA-20C ensemble members. The extremely dry years in CERA-20C are generally associated with large negative anomalies in total column water vapor. Conversely, the extremely wet years were typically associated with large positive column water vapor anomalies. Both relationships are more concordant in recent years, with exceptions mainly limited to before 1940. However, neither large positive anomalies nor large negative anomalies guarantee the emergence of corresponding precipitation anomalies in CERA-20C.

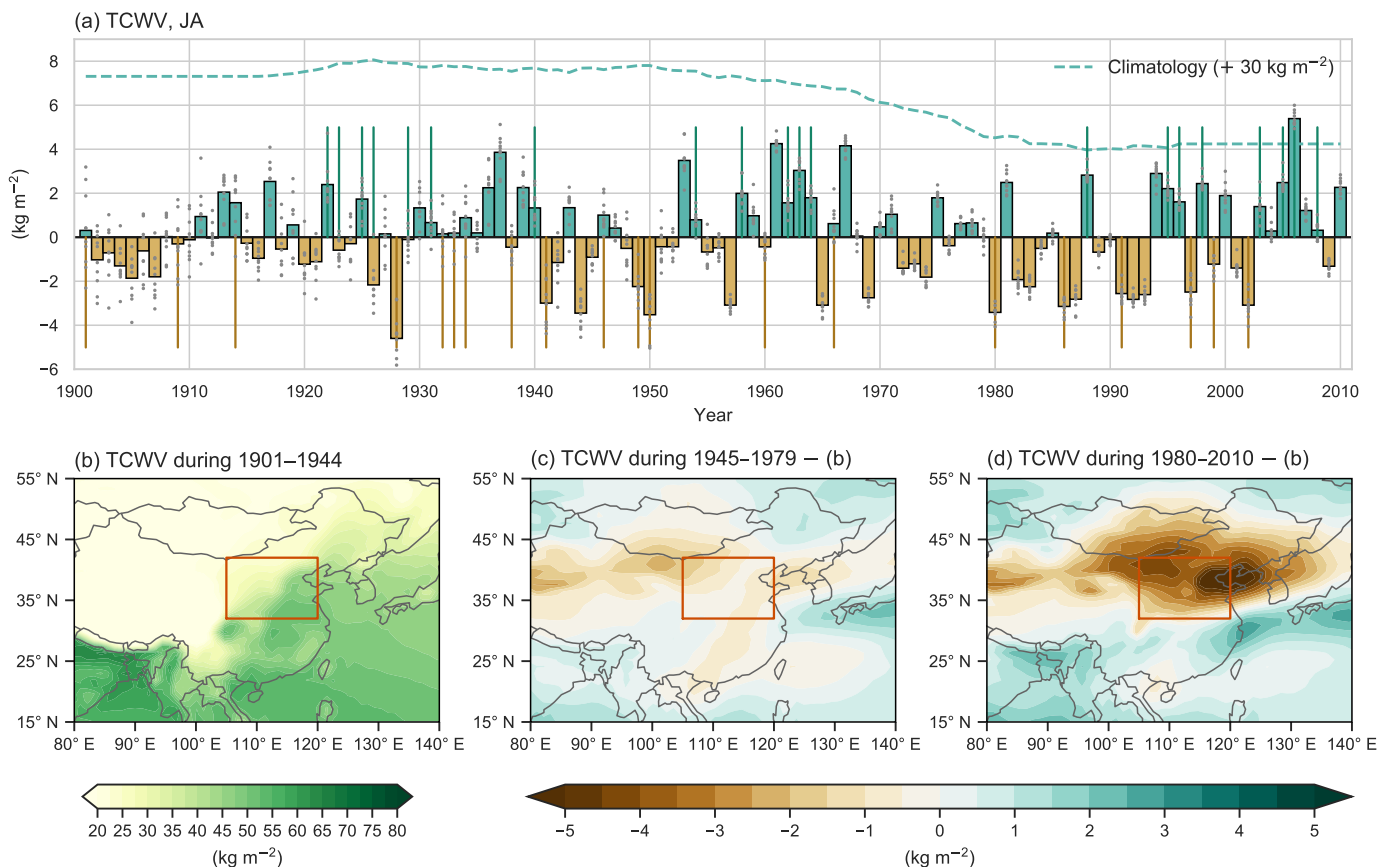


Figure 3. (a) Time series of July–August area-mean total column water vapor anomalies over North China based on the CERA-20C ensemble mean during 1901–2010. The 30-year rolling climatology is also shown for context. (b) Spatial pattern of climatological mean total column water vapor in July–August during 1901–1944. Differences during (c) 1945–1979 and (d) 1980–2010 relative to the distribution shown in (b).

Spatial patterns of climatological mean July–August total column water vapor from CERA-20C during the three time periods are shown in Figure 3b–d. The climatological mean total column water vapor decreases from the southeast to the northwest over North China, similar to the geographical distribution of precipitation (Figure 3b). The difference between the middle period (1945–1979) and the early period (1901–1944) reveals a zonal belt of decreases in the total column water vapor along 40° N, perhaps owing to reduced water vapor transport by the westerly jet. A weaker meridional belt of decreases in total column water vapor from southwest to northeast China suggests further reductions in water vapor transport from the South China Sea and Bay of Bengal (Figure 3c). During 1980–2010, the climatological mean total column water vapor in CERA-20C is substantially reduced relative to the early period across all of northern China (Figure 3d). The largest decreases are centered over Bohai Bay in the northeast, extending westward across Inner Mongolia to the Tarim Basin in the northwest. By contrast, slight increases in total column water vapor extend from the lower reaches of the Yangtze River Valley eastward across Kyushu and along the southeastern coast of Japan.

Year-by-year variations in the vertical distributions of July–August mean zonal, meridional, and vertical moisture advection during 1901–2010 are presented in Figure 4. Zonal moisture advection ($-u\partial_x q$) plays an important role in moisture supply in the lower to middle troposphere, while meridional moisture advection ($-v\partial_y q$) is mainly confined to levels between the surface and 750 hPa (Figure 4a,b). Figure 4a shows reduced zonal moisture advection in the lower troposphere ($p > 700$ hPa) starting around 1970, which coincides well with the simulated precipitation decrease over the last few decades (Figure 1a). A concomitant increase in zonal moisture advection in the middle troposphere (400–700 hPa) suggests this change represents a shift in the zonal advection term toward higher altitudes. No similar reduction or shift is evident in the meridional moisture advection term. The vertical moisture advection ($-\omega\partial_p q$) indicates strong convergence into the region during the 1950–1965 wet period and weaker convergence during the dry period after 1980 (Figure 4c).

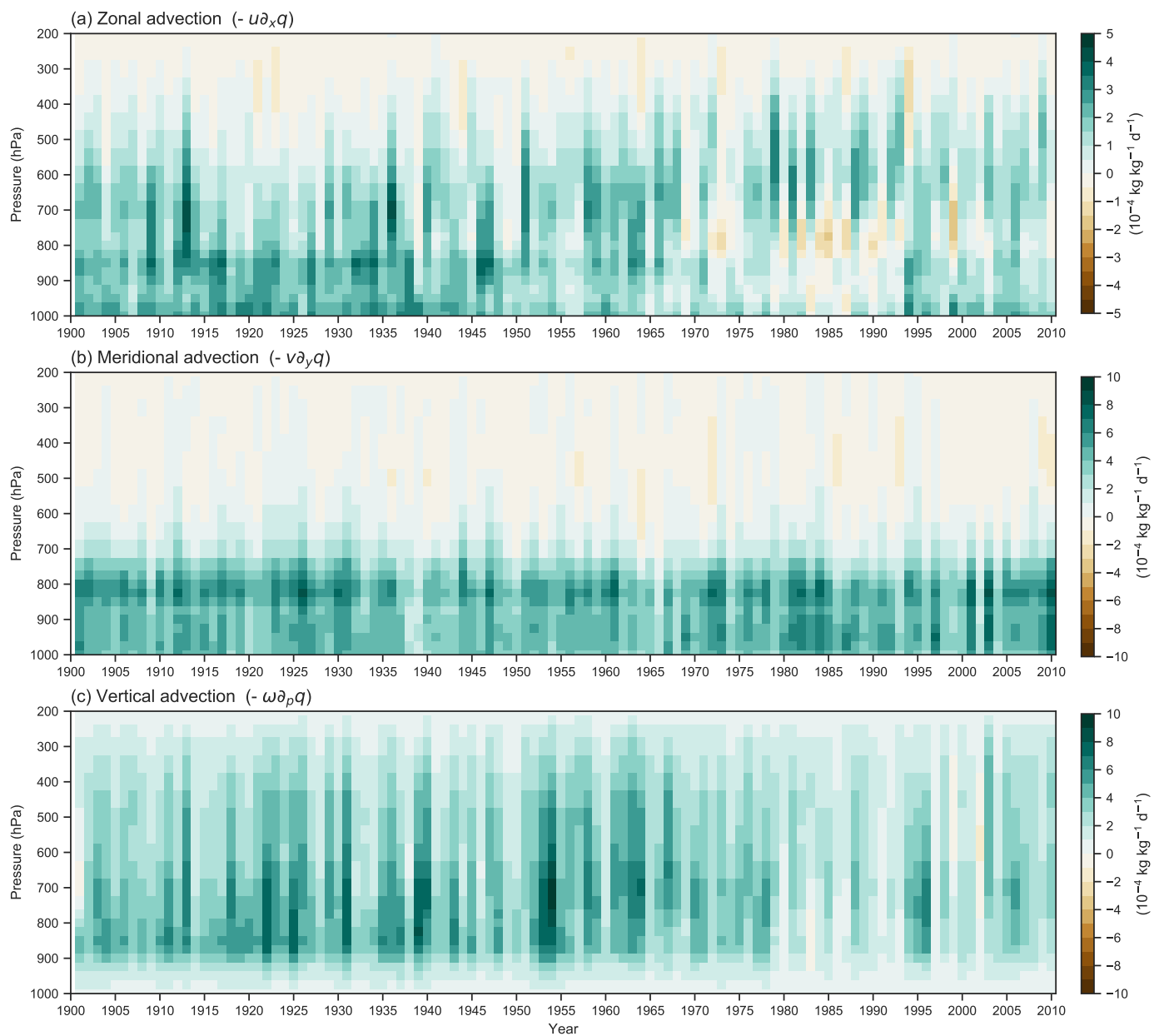


Figure 4. Interannual variations in vertical profiles of July–August mean (a) zonal, (b) meridional, and (c) vertical advection of water vapor averaged over North China in 23 layers between 1000 hPa and 200 hPa.

Figure 5a shows July–August anomalies of area-mean vertically-integrated moisture budget components relative to the 30-year running climatology in North China. Summer precipitation anomalies during 1901–2010 are generally well explained by anomalies in vertically integrated moisture flux convergence (i.e., $-\langle u\partial_x q \rangle' - \langle v\partial_y q \rangle' - \langle \omega\partial_p q \rangle'$). Biases in the magnitudes of moisture flux convergence anomalies relative to those of precipitation anomalies arise because our monthly mean analysis neglects the contributions of transient eddies. Anomalies in evaporation are small relative to anomalies in precipitation or moisture flux convergence.

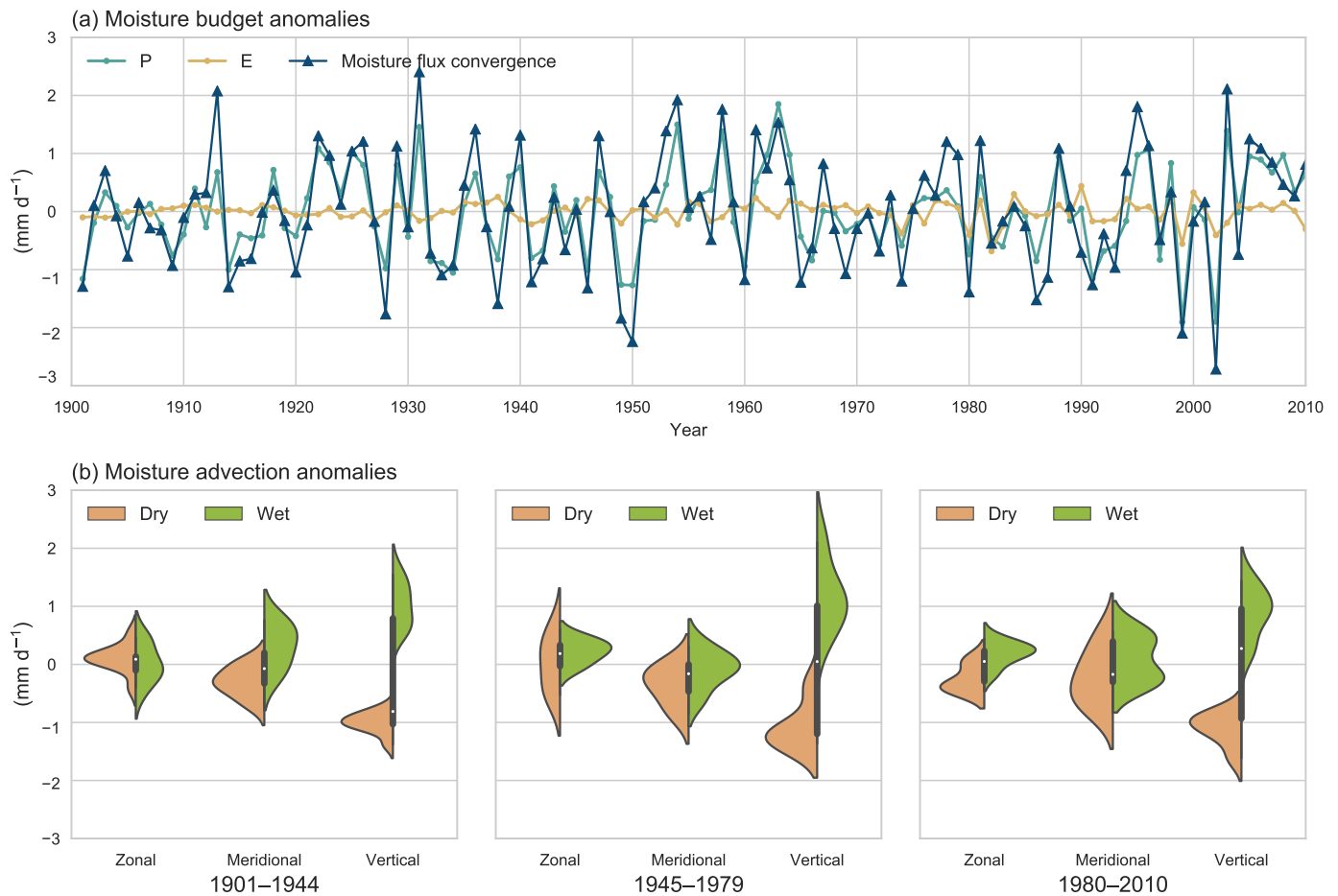


Figure 5. (a) Time series of July–August anomalies in area-mean moisture budget components (light green: precipitation; yellow: evaporation; dark blue: moisture flux convergence) over North China based on the CERA-20C ensemble mean during 1901–2010. (b) Distributions of zonal, meridional and vertical moisture advection anomalies for dry (brown) and wet (green) years during the (left-to-right) 1901–1944, 1945–1979, and 1980–2010 periods, respectively.

Distributions of anomalies in zonal, meridional, and vertical moisture advection for selected dry and wet years during 1901–1944, 1945–1979, and 1980–2010 are shown from left to right in Figure 5b. Vertical advection anomalies are consistently strong and positive in wet years and strong and negative in dry years during all three time periods. The zonal and meridional terms show weaker distinctions between dry and wet years, although both terms do tend to be more positive during wet years and the meridional term tends to be more negative during dry years. Negative zonal advection anomalies are only evident for dry years during the last period (1980–2010). Overall, precipitation deficits during dry years can be attributed to reduced meridional and vertical moisture advection, in good agreement with previous results [33]. To leading order, variations in the meridional term are linked to northward inflow across the southern boundary via the EASM circulation

and variations in the vertical term are associated with moisture convergence in the lower troposphere above North China.

3.2.2. Surface Energy Budget

Analysis of the surface energy budget helps to clarify local surface and cloud feedbacks associated with summer precipitation variability in CERA-20C. Time series of July–August surface energy flux anomalies averaged over North China are shown in Figure 6. In the surface energy budget, the downward net solar radiation (SR) flux is balanced by the sum of the upward net thermal radiation (TR), sensible heat (SH), and latent heat (LH) fluxes. The 30-year running climatological mean downward (negative) net surface SR (green dashed line in Figure 6a) shows a reduction in SR absorbed at the surface during the 1950–1970 wet period followed by an increase in SR absorbed at the surface during the post-1980 dry period. These changes are consistent with the expected response to cloud cover fluctuations associated with positive and negative precipitation anomalies, respectively. Positive and negative anomalies in the downward SR flux are likewise significantly anticorrelated with precipitation anomalies in wet and dry years ($r = 0.86$). The climatological mean upward (positive) surface TR flux (green dashed line in Figure 6b) exhibits a clear increasing trend since the late 1970s. Variations in this flux represent a balance between changes in surface emission (TR tends to increase with increasing surface temperature) and back radiation from the atmosphere (TR tends to decrease with increasing temperature or greenhouse gas concentrations in the lower troposphere). That TR increases after 1970 despite prescribed increases in carbon dioxide and other greenhouse gases [37] can be explained by the combination of a warmer surface (consistent with increased SR ; Figure 6a) and a drier atmosphere (Figure 3a). Variations in the surface SH flux climatology (Figure 6c) are broadly consistent with those in the surface TR flux, but with a more evident reduction during the wet period 1950–1970. Like the late twentieth century increase in TR , the increase in SH is attributable in part to a warmer surface. However, whereas the increase in TR is associated with a drier atmosphere, the increase in SH is associated with a drier surface. Evidence of a drier surface also manifests in a substantial decrease in surface LH flux over the latter half of the twentieth century (Figure 6d). This decrease in LH is qualitatively consistent with the reduction in precipitation over the same period (Figure 1a), and its magnitude ($\sim 15 \text{ W m}^{-2}$) is equivalent to roughly half of the 1 mm d^{-1} decrease in the 30-year running precipitation climatology over the same period.

Long-term changes in climatological surface energy fluxes based on CERA-20C thus indicate shifts toward a drier atmosphere, reduced cloud cover, and a drier and warmer surface in North China since the late 1970s. In terms of anomalies from the 30-year running climatology, extremely dry years are generally associated with a larger downward net SR flux, increased upward net TR and surface SH fluxes, and a reduced surface LH flux. Surface energy fluxes during wet years have opposite anomalies to those during dry years.

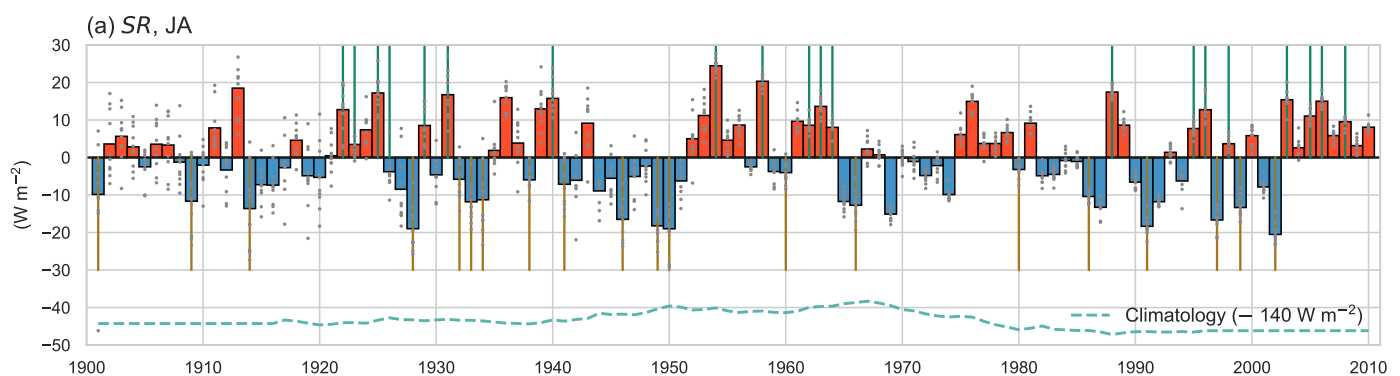


Figure 6. Cont.

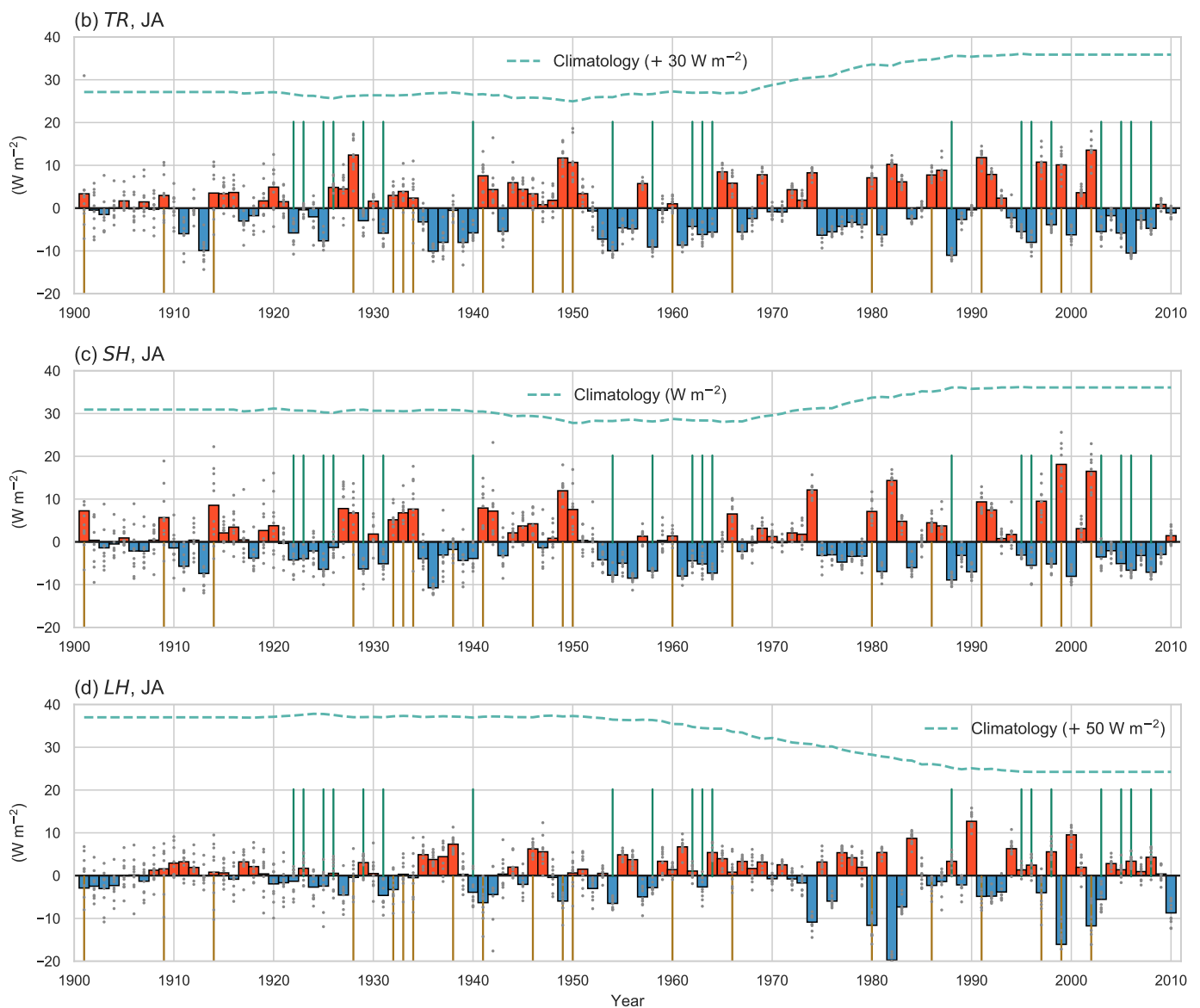


Figure 6. Time series of July–August area-mean anomalies in (a) net surface solar radiation flux, (b) net surface thermal radiation flux, (c) surface sensible heat flux, and (d) surface latent heat flux in North China based on CERA-20C ensemble during 1901–2010. The 30-year running climatology for each variable is included for context.

3.3. Long-Term Relationships between Potential Drivers and Summer Precipitation

3.3.1. Regional Circulation Patterns

Previous studies have found that upper-tropospheric cooling along the EAWJ and low-level northerly winds associated with a weak EASM are among the key circulation anomalies responsible for precipitation deficits in North China during summer [32,33,45]. Figure 7 shows time series of July–August mean climate indices representing upper tropospheric temperature (UTT), north-south displacement of the EAWJ, and the intensities of the low-level EASM and WPSH circulations based on the CERA-20C ensemble. The 30-year running climatology of UTT shows an evident cooling trend in the upper troposphere over the latter half of the twentieth century (green dashed line in Figure 7a). This cooling trend occurs in tandem with a southward displacement of the EAWJ (purple dashed line in Figure 7a). Changes in the low-level circulation (Figure 7b) show a long-term weakening of the EASM (blue dashed line) and an intensification of the WPSH (orange dashed line). The latter change is an expected consequence of global warming. This global warming

signal and the existence of systematic biases between different datasets have motivated the use of eddy geopotential height (calculated as the local geopotential height minus the zonal mean geopotential height) for describing the WPSH [44]. If the WPSH is redefined in this way (orange dotted line), then the climatology is fairly steady in time, with a mid-twentieth century peak followed by a slight weakening. Upper tropospheric cooling, a southward migration of the EAWJ, and a weakening of the EASM are all consistent with decadal decreases in summer precipitation over North China.

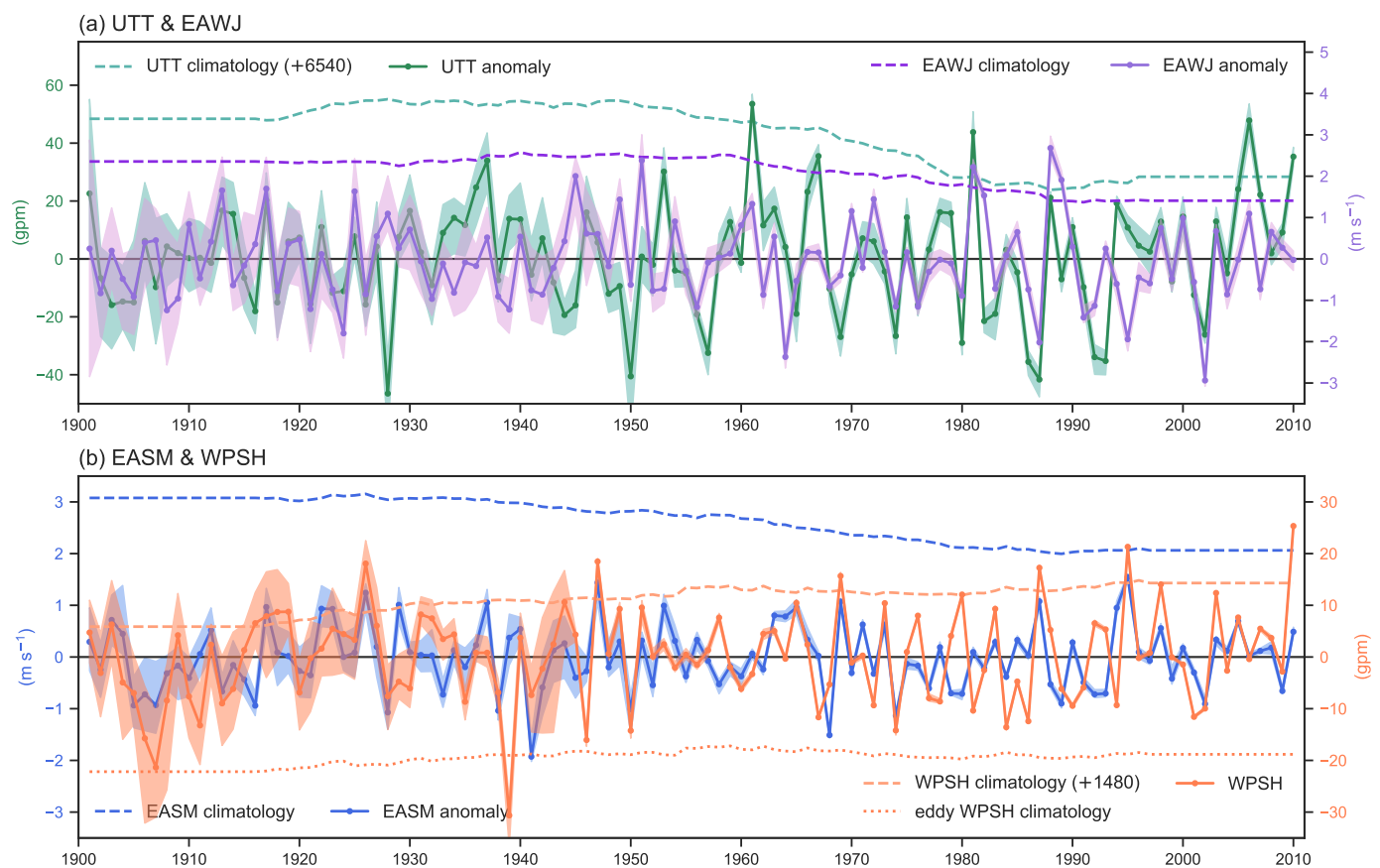


Figure 7. Time series of July–August indices of (a) upper-tropospheric temperature (UTT) and the East Asian westerly jet (EAWJ), and (b) the East Asian summer monsoon (EASM) and western Pacific subtropical high (WPSH) based on the CERA-20C ensemble mean during 1901–2010. Shaded areas indicate the spread of the ten ensemble members. The orange dotted line in (b) is the eddy WPSH index, calculated as the difference between the WPSH index and mean geopotential height within the 0–40° N latitude band.

Anomalies from the running climatologies in all four indices exhibit substantial variability at interannual time scales (solid lines in Figure 7). Anomalies in the EASM and WPSH indices show strong positive correlations across all three time periods, with correlations of 0.42, 0.61, and 0.43, respectively. Anomalies in the UTT and EAWJ indices are also closely related during 1980–2010 ($r = 0.49$), but cross-correlations are not statistically significant during the earlier periods ($r = 0.23$ during 1901–1944; $r = 0.22$ during 1945–1979). Correlation coefficients between these climate indices and summer precipitation anomalies in North China are listed in Table 1. All four indices have strong positive correlations with summer precipitation anomalies during the recent period (1980–2010), but only the EASM index shows significant correlations before 1979. Correlations between the low-level EASM circulation index and summer precipitation anomalies in North China are consistently positive for both CERA-20C and CRU during all three periods, although they only reach the 90% confidence level during the middle period (1945–1979).

Table 1. Correlation coefficients between climate indices and CERA-20C summer precipitation. Statistical significance at the 95% or greater confidence level is indicated by bold text; 90% confidence is indicated by italics. Values in brackets are correlations between climate indices and CRU summer precipitation.

Indices	1901–1944	1945–1979	1980–2010
UTT	+0.03 (+0.08)	+0.27 (+0.06)	+0.65 (+0.47)
EAWJ	+0.07 (+0.06)	−0.14 (−0.15)	+0.46 (+0.43)
EASM	+0.46 (+0.37)	+0.28 (+0.25)	+0.50 (+0.48)
WPSH	+0.05 (+0.01)	+0.29 (+0.31)	+0.36 (+0.38)
PJ	+0.26 (−0.10)	−0.19 (−0.47)	−0.50 (−0.58)
CGT	+0.09 (+0.19)	−0.07 (+0.29)	+0.05 (+0.16)
EU	−0.22 (+0.04)	−0.06 (+0.06)	−0.56 (−0.58)
Niño 3.4	+0.24 (−0.08)	−0.03 (−0.29)	−0.32 (−0.38)

In summary, CERA-20C indicates that dry years in recent decades are associated with a colder upper troposphere, a southward displacement of the EAWJ, a weaker EASM, and a weaker WPSH, in good agreement with published results [32,33,45]. However, except for the link with the EASM low-level circulation, these relationships are not consistently reproduced by CERA-20C in earlier periods.

3.3.2. Teleconnection Patterns

Composite 200-hPa geopotential height anomalies for wet and dry years during the 1901–1944, 1945–1979, and 1980–2010 sub-periods are shown in Figure 8. Wet and dry years during the early period (1901–1944) are dominated by symmetric patterns of zonal circulation anomalies along the westerly jet around 40° N (Figure 8a,d). By contrast, wet and dry years do not show symmetric circulation anomalies at upper levels during the middle (1945–1979) or late (1980–2010) periods. Composite geopotential height anomalies associated with dry years during 1945–1979 (Figure 8e) show a series of alternating anomalies aligned in the meridional direction, which may be linked to SST anomalies over the North Pacific [13]. Composite geopotential height anomalies associated with dry years during 1980–2010 (Figure 8f) show a positive EU-like wave train in the upper troposphere, in good agreement with previously published results [5,33]. Meanwhile, composite anomalies associated with wet years during 1980–2010 (Figure 8c) show a significantly enhanced South Asian high at 200 hPa. Although this result appears inconsistent with results linking eastward extension of the upper-level high to dry conditions in North China [47,48], it does match the expected response of the monsoon high to enhanced precipitation in East Asia [49]. Regardless, this enhancement of the upper-level South Asian high during wet years does not manifest as a significant feature in previous periods (Figure 8a,b).

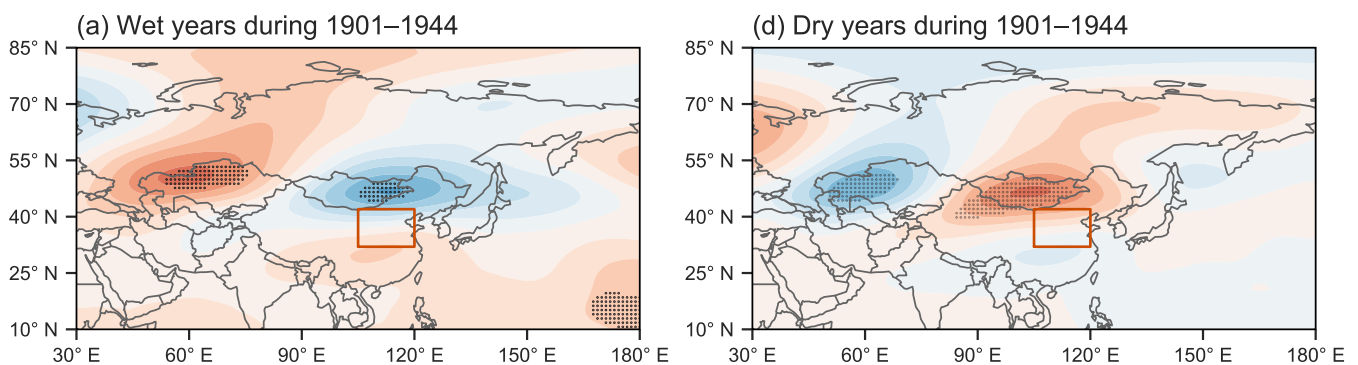


Figure 8. Cont.

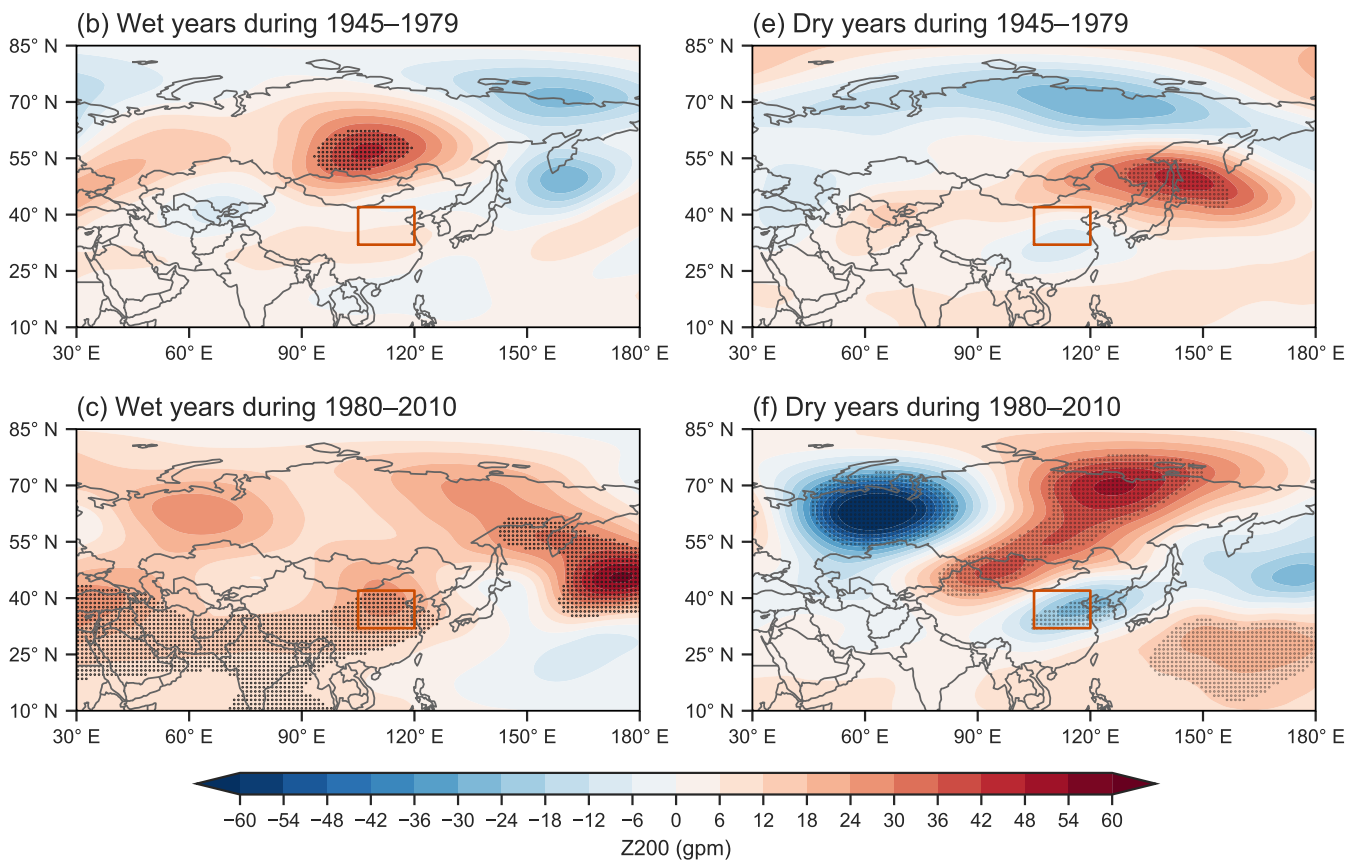


Figure 8. Spatial patterns of composite July–August geopotential height anomalies at 200 hPa for (a–c) wet years and (d–f) dry years during three different periods: (a,d) 1901–1944, (b,e) 1945–1979, and (c,f) 1980–2010 based on the CERA-20C ensemble mean. Stippling indicates that anomalies are statistically significant at the 95% confidence level.

To provide further context, we investigate long-term relationships between summer precipitation anomalies in North China and the PJ, CGT, and EU teleconnection patterns (see Section 2 for index definitions). Examination of multiple reanalysis products has suggested that these three teleconnection patterns were associated with a series of summer droughts that occurred in North China during 1980–2017 [33].

Figure 9 shows 30-year sliding correlation coefficients between the three teleconnection patterns and summer precipitation anomalies in North China. Correlations between the PJ index and precipitation anomalies based on the CERA-20C ensemble shift from positive to negative around the 1950s, suggesting asymmetric relationships during the early and latter part of the twentieth century (Figure 9a). Correlations between the ensemble mean PJ index and CRU precipitation are more consistent in sign, but temporal variability in the sliding correlation is otherwise similar to that based solely on CERA-20C. Although correlations between the CERA-20C CGT pattern index and precipitation anomalies do not reach the threshold for statistical significance, decadal changes in the sliding correlation time series suggest that this relationship may be modulated by phase shifts in the PDO (Figure 9b). Correlations with the EU pattern are consistently weak until the mid-1970s and are only significant after 1980 (Figure 9c). These results show that relationships between these large-scale teleconnection patterns and summer precipitation in North China are nonstationary in the CERA-20C reanalysis, with the expected relationships only evident since the 1980s.

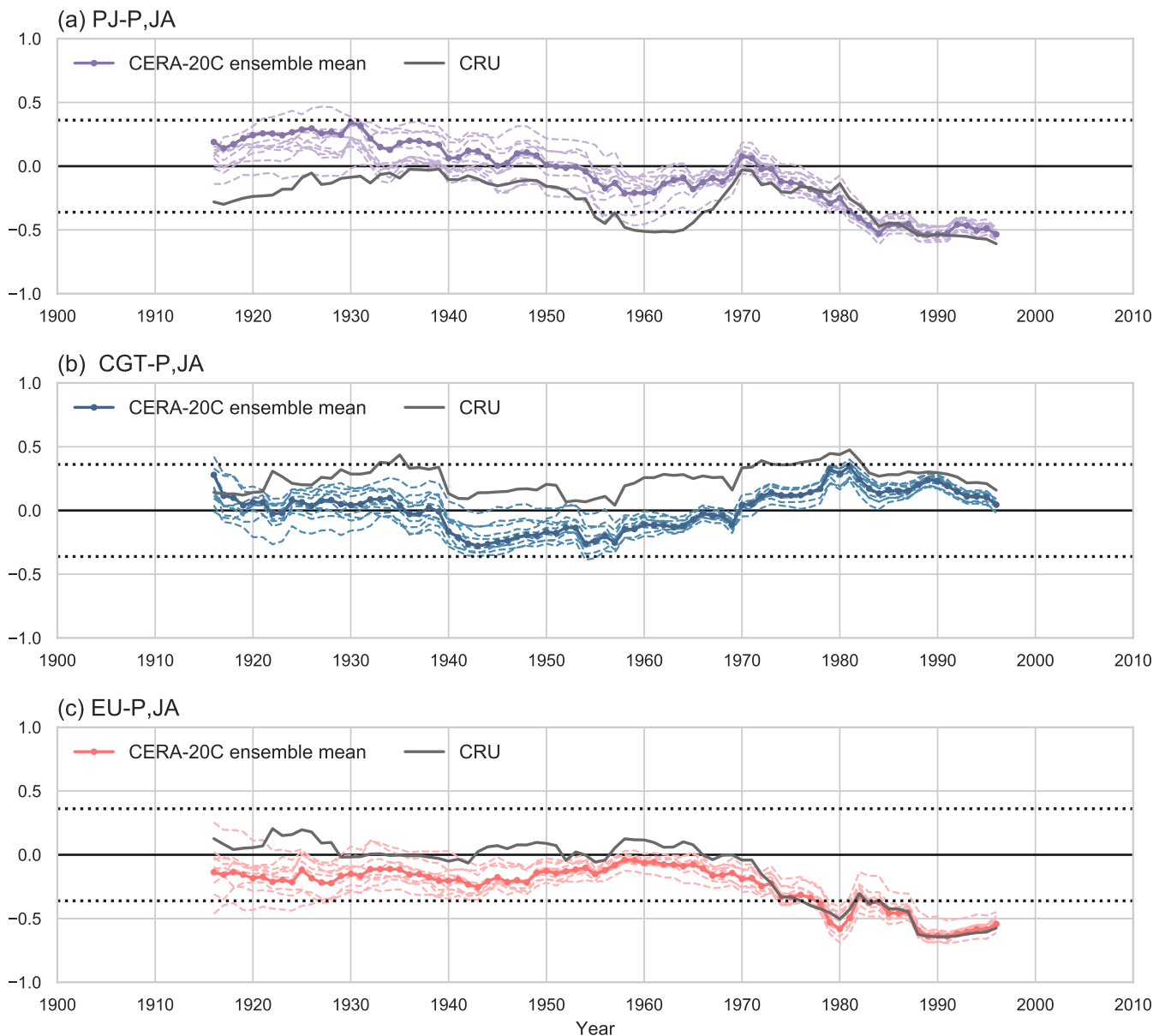


Figure 9. Thirty-year sliding correlations between summer precipitation anomalies in North China and the (a) Pacific–Japan (PJ), (b) circumpolar teleconnection (CGT), and (c) Eurasian (EU) indices based on the CERA-20C ensemble (color) and CRU precipitation estimates (grey). Circulation indices for CRU precipitation are based on the CERA-20C ensemble mean.

3.3.3. Oceanic Forcing

The PDO has been identified as a leading factor behind decadal variations in East Asian climate [14], with the phase shift of the PDO from negative to positive around the late 1970s believed to have played a dominant role in the recent weakening of the EASM. Figure 10a shows a time series of the July–August mean PDO index based on CERA-20C. The PDO index shows significant decadal variations over the past century, including predominantly negative values during 1945–1979 and positive values since 1980. ENSO is likewise believed to play an important role in the interannual variability of summer precipitation in North China [24]. A time series of the July–August mean Niño 3.4 index based on the CERA-20C ensemble is shown in Figure 10b. As expected, dry years often occur in tandem with distinctive ENSO signals in CERA-20C; however, the ENSO phase associated with dry years is not consistent over time in this reanalysis. Figure 10c shows 30-year sliding correlation coefficients between the Niño 3.4 index and

summer precipitation anomalies in North China during July–August. This time series shows a remarkable shift from positive correlations over the first four decades of the reanalysis to negative correlations over the last three decades. This shift is similar to that in correlations against the PJ index (Figure 9), in keeping with the role of PJ anomalies in linking ENSO influences to summer precipitation in East Asia [50]. Significant negative correlations with ENSO variability are identified for both CERA-20C and CRU precipitation estimates near the end of the reanalysis record.

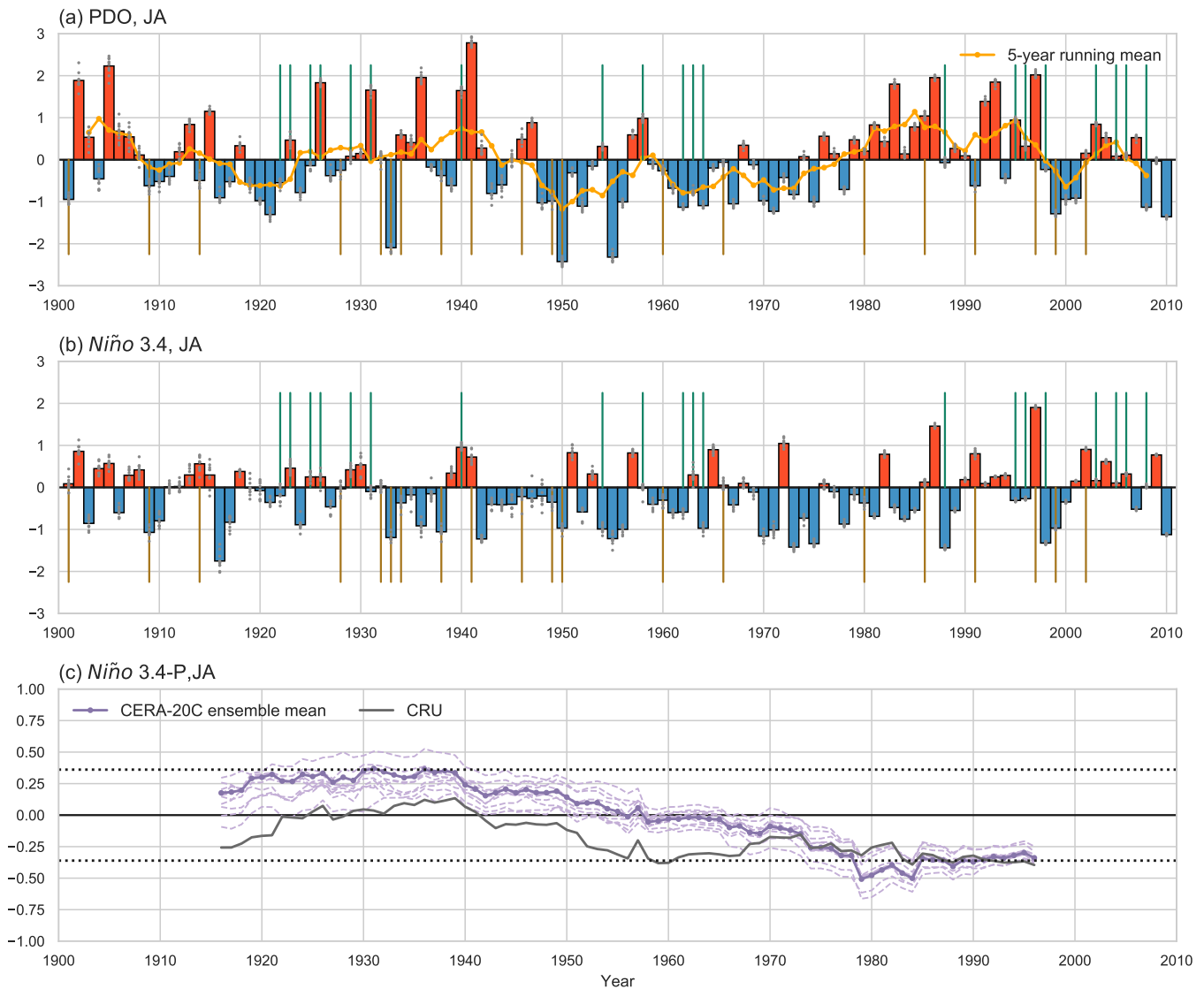


Figure 10. Time series of July–August (a) Pacific decadal oscillation (PDO) and (b) Niño 3.4 indices during 1901–2010. (c) Thirty-year sliding correlations between the Niño 3.4 index and summer precipitation anomalies in North China based on the CERA-20C ensemble (purple) and CRU precipitation estimates (grey).

3.3.4. Synthesis Evaluation of Large-Scale Drivers

Figures 8–10 show that statistical relationships between several large-scale circulation indices and precipitation anomalies in North China are nonstationary in the CERA-20C reanalysis. To further illustrate this nonstationarity, we use multiple linear regression to summarize and roughly quantify fits between the evaluated large-scale circulation indices and summer precipitation anomalies in North China in the context of CERA-20C. Figure 11 compares CERA-20C summer precipitation anomalies against expected anomalies based on multiple linear regression onto standardized indices for each of the three analysis

periods. Both the precipitation anomalies and the standardized indices are based on the CERA-20C ensemble mean. All potential drivers with significant linear correlations to summer precipitation anomalies during at least one of the sub-periods (i.e., all but CGT; Table 1) are selected to conduct the linear regression.

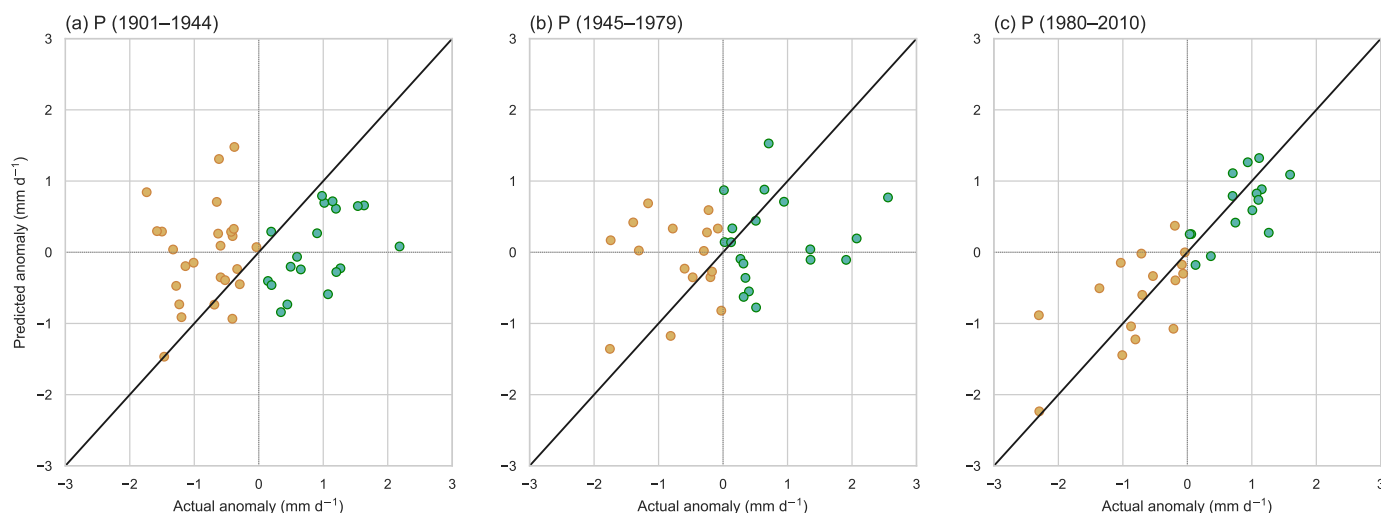


Figure 11. Multiple linear regressions of summer precipitation anomalies onto standardized climate indices for the (a) 1901–1944, and (b) 1945–1979, and (c) 1980–2010 periods based on the CERA-20C ensemble mean. Years with negative precipitation anomalies are shown in brown, positive precipitation anomalies in green. All fitting coefficients are based on the 1980–2010 period.

We first conduct the regression for the 1980–2010 period, as many studies linking these potential large-scale drivers to precipitation anomalies in North China are based either entirely [6,21,33] or in large part [20,22,32] on data from these recent decades. In keeping with the results outlined above, the simple linear model performs well for this period. Linear combination of the evaluated indices explains 72% of interannual variability in July–August precipitation anomalies over North China during 1980–2010 ($r = 0.85$; $p < 0.001$). Ranked by absolute magnitude of coefficient, the PJ (coefficient: -0.53) and UTT (0.45) indices are selected as the most discriminating variables for precipitation anomalies during this period, followed by Niño 3.4 (0.28). However, we have not controlled for cross-correlations among the indices. These relative magnitudes should therefore be treated as illustrative rather than explanatory.

For the earlier periods, we adopt two complementary approaches. First, we conduct similar multiple linear regressions for the 1901–1944 and 1945–1979 periods, training the models on data from each period independently. The regressions yield identical correlation coefficients between predicted and simulated anomalies ($r = 0.55$; $p < 0.001$) for both periods in CERA-20C, indicating that linear combinations of these indices can explain around 30% of the interannual variability in precipitation over North China. For an alternate perspective, we apply the multiple linear regression model derived for 1980–2010 directly to data from the 1901–1944 and 1945–1979 periods. This latter approach, the results of which are shown in Figure 11a,b, is analogous to treating the earlier periods as test samples for a model trained on data for recent decades. The resulting correlation coefficients between predicted and simulated precipitation anomalies are 0.19 for 1901–1944 and 0.25 for 1945–1979. Neither correlation is statistically significant at the 90% confidence level. This result confirms that relationships based on 1980–2010 do not extend well to earlier periods in CERA-20C.

4. Discussion

We cannot assume that CERA-20C is a reliable record of historical variability, especially during the early years of the twentieth century. However, the reanalysis precipitation is

a product of the large-scale dynamics as reproduced within the data assimilation system and the interactions of these dynamical fields with the model physical parameterizations. The climatology and interannual variability of precipitation thus result from an internal consistency (governed by the model formulation) that is constrained to evolve in ways that do not deviate too far from the observed state (governed by the data assimilation). The broadly similar temporal evolutions in relationships between potential large-scale drivers and summer precipitation anomalies in North China among the ten individual ensemble members (Figures 9 and 10) are therefore instructive, as they affirm that changes in data assimilation constraints contribute substantially to changes in the relationships between large-scale circulation indices and precipitation in North China. However, it is not immediately clear to what extent this similarity derives from changes in the strength of the data assimilation (i.e., the quantity and quality of assimilated data) versus actual changes in the relationships (i.e., real variability that enters the reanalysis via data assimilation). The first explanation would indicate that the model is unable to represent the actual relationships without strong data assimilation constraints, while the second would imply that large-scale controls on summer precipitation in North China inferred from recent records may be less general than expected. Either of these conclusions implies pervasive uncertainty not only in seasonal forecasts but also in long-term model-based projections of how summer precipitation and the large-scale factors in this region will evolve under climate change.

It is helpful at this point to return to the questions posed in Section 1. We start with the questions related to the performance of the underlying model and data assimilation system. The first question concerns whether relationships identified for recent decades are preserved when upper-atmospheric constraints are removed. The answer to this question is a resounding yes. The correlations listed in Table 1 confirm that expected relationships with large-scale circulation indices are reproduced well by CERA-20C during the 1980–2010 period. CGT is a possible exception; however, it has been suggested that CGT variability may serve more to modulate drought type rather than determine drought occurrence [33]. Our results, therefore, indicate that assimilation of upper-air observations is not necessary to adequately constrain relationships between large-scale circulation indices and summer precipitation in North China during recent years.

The second question concerns the performance of the system during the early part of the record when the observations available for assimilation are relatively sparse. This question requires a closer look at how the climatology and ensemble spread evolve over the early twentieth century. Several important clues are provided by evaluating the climatological mean and interannual variability of summer precipitation over North China based on CERA-20C against those from the CRU and UDEL gauge-based analyses. Figure 1a shows a positive bias of about 1 mm d^{-1} ($\sim 20\%$) in the CERA-20C precipitation rate relative to CRU and UDEL that persists through most of the twentieth century before shrinking steadily between the late 1960s and the late 1980s. Spatial distributions of the CERA-20C mean precipitation during the 1901–1944 and 1980–2010 periods show that the decrease is due largely to reduced precipitation in the northeastern part of the North China domain (Figure 2c). Correlations against observed anomalies also increase sharply around the mid-1960s in all ensemble members (Figure 1c). These changes suggest increased reliability in both the mean state and the interannual variability of summer precipitation in North China produced by CERA-20C. Figure 3a similarly shows a decrease of about 4 kg m^{-2} ($\sim 10\%$) in total column water vapor that begins around 1950, accelerates in the late 1960s, and ends in the early 1980s. The steeper decline after the late 1960s corresponds to the sharp reduction in the precipitation bias. Like the decrease in precipitation, this decline is most pronounced in the northeastern part of the domain (Figure 3d).

No direct constraints on atmospheric moisture are assimilated in CERA-20C. We, therefore, expect the reductions in precipitation and total column water vapor to reflect long-term changes in atmospheric circulation patterns, potentially supported by feedbacks in surface evaporation. Examining climatologies of the source terms in the moisture budget, we find

reductions of approximately 0.2 mm d^{-1} in vertically-integrated zonal moisture advection ($\sim 30\%$; Figure 4a), 0.1 mm d^{-1} in vertically-integrated meridional moisture advection ($\sim 10\%$; Figure 4b), and 0.5 mm d^{-1} in surface evaporation ($\sim 15\%$; Figure 6d) between the first and last 30-year periods in CERA-20C. Changes in moisture advection depend directly on the atmospheric circulation, while changes in evaporation depend mainly on the land surface model, surface winds, and the intensity of boundary layer mixing (with the latter two features also sensitive to changes in the low-level circulation). We, therefore, infer that the improved reliability of North China precipitation in CERA-20C derives from stronger data assimilation constraints on the atmospheric circulation associated with the expanded availability and spatial coverage of surface pressure observations over the 1960s and 1970s. Surface pressures assimilated over land in CERA-20C are taken from version 3 of the International Surface Pressure Databank (ISPD) over land [51]. The ISPD contains very few observations of surface pressure in East or Central Asia before 1950, and dense coverage of the region is only consistently available after 1967 [52]. It is tempting to further infer that the decrease in evaporation results from drying of the land surface in response to reduced precipitation; however, changes in evaporation lead the decrease in precipitation by nearly a decade (cf. Figures 1a and 6d). Moreover, decreases in vertically-integrated vertical moisture advection (Figure 4c) are almost identical to those in precipitation, indicating that, even though moisture transport and total column water vapor decline through the 1950s and 1960s, lower tropospheric moisture convergence is not substantially impacted until the late 1960s. The spatial distribution of changes in surface evaporation based on CERA-20C for the North China domain (not shown) indicates that the initial decrease in evaporation through the 1960s occurs mainly over open water, namely Bohai Bay in the northeastern corner of the domain and Hongze Lake in the southeast. Further decreases in evaporation during the 1970s and 1980s are then driven by the land surface response to reduced precipitation over the North China Plain, as also suggested by the timing of changes in surface radiation and sensible heat fluxes (Figure 6).

The marked improvement of precipitation and its variability starting from the late 1960s indicates that relationships identified in the early part of the CERA-20C record are unreliable. Data assimilation constraints provided by observations in other parts of the world (and especially the similar evolutions of SST anomalies) are sufficient to produce broadly similar statistical relationships across the ensemble, but we cannot treat these relationships as indicative of historical co-variability between the large-scale indices and precipitation. Laloyaux et al. [37] proposed an ensemble-based confidence metric that helps to illustrate this issue. This metric is defined as 1 minus the ratio of ensemble spread to climatological variability, defined, respectively, as the square root of the 30-year running mean of the ensemble variance and the 30-year running standard deviation of the ensemble mean. This confidence metric is often negative in the early twentieth century (negative values indicate that ensemble spread exceeds climatological variability), and does not consistently exceed 0.5 until around 1950. The relationships identified for the early period (1901–1944), which suggest symmetric anomalies along the northern flank of the subtropical jet for wet and dry years (Figure 8a,d), may therefore reflect controlling patterns of summer precipitation anomalies in the weakly constrained atmospheric model. Sliding correlations of CERA-20C precipitation anomalies against CRU and UDEL also do not consistently exceed the 95% confidence threshold until around 1950 (Figure 1c). Although the gauge-based analyses are also subject to large uncertainties in the early part of the twentieth century, these poor correlations suggest that, even to the extent that the large-scale circulation patterns are constrained by observations elsewhere, their relationships with summer precipitation anomalies in North China are not well represented until regional constraints are available.

Although positive biases in regional summer precipitation relative to CRU and UDEL persist through most of the middle period (1945–1979), sliding 30-yr correlations for interannual anomalies between CERA-20C and the observational analyses are strong and significant through all but the first few years of this period. Given this improved fidelity,

different relationships between large-scale circulation indices and North China summer precipitation between the middle and late periods may reflect actual nonstationarity in the factors driving regional precipitation variability. Given its role in modulating East Asian climate, the PDO could provide a plausible basis for this nonstationarity [13,14]. To investigate this possibility, we have repeated the multiple linear regression analysis (Section 3.3.4) using data composited on the phase of the PDO rather than the three periods, focusing on the 1950–2010 period for which interannual anomalies based on CERA-20C agree well with those based on CRU and UDEL (Figure 1c). Here, we assign a year to the positive PDO category if the JA-mean PDO index exceeds 0.5 (total 15 years), to the negative PDO category if the JA-mean PDO index is less than -0.5 (20 years), and to the neutral category if the JA-mean PDO index is within ± 0.5 (26 years). Correlation coefficients between the regression results and the simulated CERA-20C anomalies are consistent and significant at the 99% confidence level for all three classes, ranging from 0.74 for negative PDO years to 0.80 for neutral years. For positive PDO years, the regression relies mainly on the UTT (positive), PJ (negative), and EU (negative) indices. A regression based solely on these three indices provides a statistically equivalent fit to the CERA-20C anomalies during positive PDO years ($r = 0.79$; $p < 0.001$). For negative PDO years, the EASM index (positive) is the main contributor to the regression result. This index alone can explain 48% of the linear variability ($r = 0.69$; $p < 0.001$) in CERA-20C anomalies during negative PDO years. The result for neutral PDO years is similar to that for positive PDO years but with a larger role for the PJ index and a near-zero coefficient for the EU index. The results for negative and positive PDO years are broadly consistent with differences between the middle and late periods (as summarized in Table 1 and Section 3.3.4); however, this analysis and that shown in Figure 11b,c are not mutually exclusive because the PDO index was predominantly negative during 1945–1979 and predominantly positive during 1980–2010 (Figure 10a). Sensitivity simulations in an atmospheric model that has been shown to simulate North China summer precipitation and its variability well would help to evaluate these possibilities more fully.

We are now able to address the remaining pair of questions, which concern the long-term viability of hypotheses developed based on data for recent decades. First, does the full reanalysis record support the hypothesis? With the exception of the EASM, which maintains consistent positive correlations at the 90% or greater confidence level for all three periods, the answer to this question is no. Among the most striking deviations from the expected relationships, correlations against Niño 3.4 (and PJ) change sign from positive in the early twentieth century to negative in recent decades (Figure 10c) and no significant correlation with the EU index is evident prior to the late 1970s. This leads then to the second question: do deviations from the hypothesis appear to arise mainly from actual variations in the climate system or from shortcomings of the reanalysis framework? The mid-twentieth century sign changes in the Niño 3.4 and PJ correlations most likely result from shortcomings in the reanalysis system. As detailed above, regional responses to large-scale forcings in CERA-20C are unreliable until the introduction of consistent local observations in the middle of the twentieth century. Moreover, correlations of both indices against CRU precipitation anomalies in the 1950s and 1960s are comparable to those in recent years, suggesting that the weak relationships indicated by CERA-20C during this period may be in error. By contrast, the relatively recent emergence of the relationship with the EU index could reflect actual nonstationarity in the large-scale factors influencing summer precipitation in North China, as indicated by the similar evolution of correlations between the EU index and CRU. Explanations for this change could include the PDO phase shift from negative to positive in the 1970s or changes in the EU pattern associated with recent changes in Arctic sea ice or Eurasian snow cover. The latter hypothesis is more consistent with the lack of relationship in the early part of the twentieth century; however, the weak relationship during this period may also simply reflect the correspondingly weak constraints on CERA-20C. Although we cannot entirely rule out the possibility that the weak relationship between the CERA-20C EU index and CRU precipitation anomalies

in the 1950s and 1960s results from a poor representation of EU pattern variability in CERA-20C during this period, variations in the CERA-20C EU index are nearly identical to those based on the full-input Japanese 55-year Reanalysis over 1958–1972 ($r = 0.97$).

5. Conclusions

We have evaluated the long-term variability of relationships between summer precipitation anomalies in North China and their potential large-scale drivers in the CERA-20C reanalysis covering 1901–2010. The 30-year running climatology of the CERA-20C ensemble mean captures observed decadal shifts in summer precipitation in North China around the mid-1940s and late 1970s, despite a persistent positive bias relative to observations prior to 1980 (Figure 1a). The shift in the late 1970s, which reflects both a real shift toward drier conditions and a reduction in the CERA-20C bias relative to observations, is related to decreased zonal moisture advection in the lower troposphere and suppressed vertical moisture advection (Figure 4). These changes are likewise associated with a shift toward a drier atmosphere (Figure 3) and a drier and warmer surface (Figure 6) since the late 1970s. Large-scale factors associated with these changes include a cooling of the upper troposphere above East Asia and a southward migration of the EAWJ (Figure 7a), a weakening of the EASM and WPSH (Figure 7b), and a phase transition of the PDO from negative to positive (Figure 10a).

Interannual variability of summer precipitation and associated changes in the atmospheric moisture and surface energy budgets have been investigated based on July–August anomalies calculated from the ten CERA-20C ensemble members. We have focused on three distinct periods according to changes in the precipitation climatology (Figures 1 and 2): 1901–1944 (early/neutral), 1945–1979 (middle/wet), and 1980–2010 (late/dry). Summer precipitation and associated circulation anomalies show symmetric characteristics for wet versus dry years during 1901–1944 (Figures 2d,g and 8a,d). By contrast, upper-level circulation anomalies associated with wet and dry years during 1980–2010 are not symmetric (Figure 8c,f). Wet years during this period are associated with an intensified and elongated South Asian high, while dry years are associated with the positive phase of the EU teleconnection pattern. Neither feature is evident in corresponding wet and dry composites for the 1901–1944 or 1945–1979 periods. The atmospheric moisture budget indicates that precipitation deficits during dry years can be attributed primarily to reduced vertical moisture advection, with negative meridional moisture advection anomalies playing a secondary but qualitatively consistent role in all three periods (Figure 5). Zonal advection anomalies also show negative anomalies for dry years after 1980, but show no clear difference between wet and dry years during the 1901–1944 or 1945–1979 periods. The surface energy budget reveals that extremely dry years are generally associated with a larger downward net flux of shortwave radiation, larger upward net fluxes of longwave radiation and surface sensible heat, and reduced surface evaporation (Figure 6).

We have also evaluated interannual relationships between summer precipitation anomalies in North China and their potential large-scale drivers, including regional circulation patterns (UTT, EAWJ, EASM, and WPSH), hemispheric teleconnection patterns (PJ, CGT, and EU), and oceanic forcing (Niño 3.4) during the three different periods. We find substantial nonstationarity in these relationships, with most of the expected relationships based on previous work evident only since the 1980s (Figures 7–10; Table 1). The relationship with the low-level EASM is the lone exception, with positive correlations significant at the 90% or greater confidence level during all three periods. Positive relationships with the UTT, EAWJ, and WPSH indices are not consistently reproduced by CERA-20C in earlier periods, the relationship with the EU index is only evident after the late 1970s, and correlations with the PJ and Niño 3.4 indices change sign in the middle of the twentieth century.

We have discussed two possible reasons for the nonstationarity in the large-scale drivers of North China precipitation in CERA-20C (Section 4). The first possibility is that changes in the relationships arise due to limitations in the reanalysis, and particularly the influence of long-term changes in the strength of constraints provided by observational

data assimilation. This is the most convincing explanation for differences between the early (1901–1944) and late (1980–2010) periods, as the CERA-20C ensemble spread is comparable to climatological variability for much of the early period and correlations with observational estimates are poor (Figure 1c). The second possibility is that relationships between large-scale circulation patterns and precipitation anomalies in North China are in fact nonstationary in time. This hypothesis appears to explain at least some of the differences between the middle (1945–1979) and late (1980–2010) periods, particularly the emergence of significant relationships with the EU index after the late 1970s. The role of the PDO in modulating East Asian climate provides a plausible basis for the hypothesis, as the PDO phase changed from predominantly negative in the middle period to predominantly positive in the late period (Figure 10a). However, despite improved correlations and confidence metrics compared to the early neutral period, the persistence of positive biases relative to observed regional precipitation estimates prior to the 1980s (Figure 1a) suggests that evolving data assimilation constraints also contribute to differences between middle and late periods. The relative magnitudes of these two contributions remains unclear and should be evaluated further in future work based on complementary data sets and model simulations.

Author Contributions: L.D. conducted the analysis, prepared the figures, and wrote the initial draft. J.S.W. was responsible for acquiring funding and resources. Both authors were involved in conceiving the study and writing the paper. Both authors have read and agreed to the published version of the manuscript.

Funding: This research was supported by the National Key Research and Development Program of Chinese Ministry of Science and Technology (Grant No. 2017YFC1501404).

Data Availability Statement: CERA-20C products are produced by ECMWF and have been acquired from the ECMWF public archive, available online: <https://apps.ecmwf.int/datasets> (accessed on 25 September 2020). ERA5 products have been acquired from the Copernicus Climate Change Services (C3S) Climate Data Store, available online: <https://cds.climate.copernicus.eu> (accessed on 5 September 2020). CRU precipitation data are produced by the Climatic Research Unit at the University of East Anglia, and have been acquired from the United Kingdom's Centre for Environmental Data Analysis at <https://catalogue.ceda.ac.uk> (accessed on 5 September 2020). The UDEL precipitation data are produced by the University of Delaware Department of Geography and Spatial Sciences, and have been acquired from NOAA/OAR/ESRL PSL, Boulder, CO, USA from their web site at https://psl.noaa.gov/data/gridded/data.UDEL_AirT_Precip.html (accessed on 5 September 2020).

Acknowledgments: We thank three anonymous reviewers for their helpful suggestions.

Conflicts of Interest: The authors declare no conflict of interest. The funders had no role in the design of the study; in the collection, analyses, or interpretation of data; in the writing of the manuscript, or in the decision to publish the results.

References

1. Ding, Y.; Wang, Z.; Sun, Y. Inter-decadal variation of the summer precipitation in East China and its association with decreasing Asian summer monsoon. Part I: Observed evidences. *Int. J. Climatol.* **2008**, *28*, 1139–1161. [[CrossRef](#)]
2. Ding, Y.; Chan, J. The East Asian summer monsoon: An overview. *Meteorol. Atmos. Phys.* **2005**, *89*, 117–142.
3. Hua, T.; Zorita, E.; Wang, X.; Wang, N.; Zhang, C. Precipitation variability in the north fringe of East Asian Summer Monsoon during the past millennium and its possible driving factors. *Clim. Dyn.* **2019**, *53*, 2587–2602.
4. Tong, X.; Yan, Z.; Xia, J.; Lou, X. Decisive Atmospheric Circulation Indices for July–August Precipitation in North China Based on Tree Models. *J. Hydrometeorol.* **2019**, *20*, 1707–1720.
5. Wang, H.; He, S. The North China/Northeastern Asia severe summer drought in 2014. *J. Clim.* **2015**, *28*, 6667–6681. [[CrossRef](#)]
6. Wang, S.; Yuan, X.; Li, Y. Does a strong El Niño imply a higher predictability of extreme drought? *Sci. Rep.* **2017**, *7*, 40741. [[CrossRef](#)] [[PubMed](#)]
7. Yu, C.; Huang, X.; Chen, H.; Huang, G.; Ni, S.; Wright, J.S.; Hall, J.; Ciais, P.; Zhang, J.; Xiao, Y.; et al. Assessing the impacts of extreme agricultural droughts in China under climate and socioeconomic changes. *Earth Future* **2018**, *6*, 689–703.
8. Zhao, Y.; Chen, D.; Li, J.; Chen, D.; Chang, Y.; Li, J.; Qin, R. Enhancement of the summer extreme precipitation over North China by interactions between moisture convergence and topographic settings. *Clim. Dyn.* **2020**, *54*, 2713–2730.
9. Ali, R.; Kuriqi, A.; Kisi, O. Human–Environment Natural Disasters Interconnection in China: A Review. *Climate* **2020**, *8*, 48.

10. Lu, R. Interannual variation of North China rainfall in rainy season and SSTs in the equatorial eastern Pacific. *Chin. Sci. Bull.* **2005**, *50*, 2069–2073. [[CrossRef](#)]
11. Wang, H. The Weakening of the Asian Monsoon Circulation after the End of 1970's. *Adv. Atmos. Sci.* **2001**, *18*, 376–386.
12. Zhou, B.; Zhai, P.; Chen, Y. Contribution of changes in synoptic-scale circulation patterns to the past summer precipitation regime shift in eastern China. *Geophys. Res. Lett.* **2020**, *47*, e2020GL087728. [[CrossRef](#)]
13. Qian, C.; Zhou, T. Multidecadal Variability of North China Aridity and Its Relationship to PDO during 1900–2010. *J. Clim.* **2014**, *27*, 1210–1222. [[CrossRef](#)]
14. Dong, X. Influences of the Pacific Decadal Oscillation on the East Asian Summer Monsoon in non-ENSO years. *Atmos. Sci. Lett.* **2016**, *17*, 115–120.
15. Yu, R.; Wang, B.; Zhou, T. Tropospheric cooling and summer monsoon weakening trend over East Asia. *Geophys. Res. Lett.* **2004**, *31*, L22212.
16. Zhang, L.; Zhou, T. The interannual variability of summer upper-tropospheric temperature over East Asia. *J. Clim.* **2012**, *25*, 6539–6553. [[CrossRef](#)]
17. Zhu, C.; Wang, B.; Qian, W.; Zhang, B. Recent weakening of northern East Asian summer monsoon: A possible response to global warming. *Geophys. Res. Lett.* **2012**, *39*, L09701.
18. Wang, Z.; Lin, L.; Yang, M.; Guo, Z. The role of anthropogenic aerosol forcing in interdecadal variations of summer time upper-tropospheric temperature over East Asia. *Earth Future* **2019**, *7*, 136–150. [[CrossRef](#)]
19. Mu, J.; Wang, Z. Responses of the East Asian summer monsoon to aerosol forcing in CMIP5 models: The role of upper-tropospheric temperature change. *Int. J. Climatol.* **2020**. [[CrossRef](#)]
20. Huang, G.; Liu, Y.; Huang, R. The interannual variability of summer rainfall in the arid and semiarid regions of Northern China and its association with the northern hemisphere circumglobal teleconnection. *Adv. Atmos. Sci.* **2011**, *28*, 257–268.
21. Sampe, T.; Xie, S. Large-Scale Dynamics of the Meiyu-Baiu Rainband: Environmental Forcing by the Westerly Jet. *J. Clim.* **2010**, *21*, 113–134. [[CrossRef](#)]
22. Chiang, J.; Swenson, L.; Kong, W. Role of seasonal transitions and the westerlies in the interannual variability of the East Asian summer monsoon precipitation. *Geophys. Res. Lett.* **2017**, *44*, 3788–3795. [[CrossRef](#)]
23. Wang, S.; Zuo, H.; Yin, Y.; Wang, J.; Ma, X. Asymmetric impact of East Asian jet's variation on midsummer rainfall in North China and Yangtze River Valley. *Clim. Dyn.* **2019**, *53*, 6199–6213. [[CrossRef](#)]
24. Feng, S.; Hu, Q. Variations in the Teleconnection of ENSO and Summer Rainfall in Northern China: A Role of the Indian Summer Monsoon. *J. Clim.* **2004**, *17*, 4871–4881. [[CrossRef](#)]
25. Wang, H. The instability of the East Asian summer monsoon-ENSO relations. *Adv. Atmos. Sci.* **2002**, *19*, 1–11.
26. Gao, H.; Wang, Y.; He, J. Weakening significance of ENSO as a predictor of summer precipitation in China. *Geophys. Res. Lett.* **2006**, *33*, L09807.
27. Nitta, T. Convective activities in the tropical western Pacific and their impact on the Northern Hemisphere summer circulation. *J. Meteorol. Soc. Jpn.* **1987**, *65*, 373–390. [[CrossRef](#)]
28. Huang, R. The East Asia/Pacific pattern teleconnection of summer circulation and climate anomaly in East Asia. *J. Meteorol. Res.* **1992**, *6*, 25–37.
29. Kosaka, Y.; Nakamura, H. Mechanisms of meridional teleconnection observed between a summer monsoon system and a subtropical anticyclone. Part I: The Pacific-Japan pattern. *J. Clim.* **2010**, *23*, 5085–5108. [[CrossRef](#)]
30. Wallace, J.M.; Gutzler, D.S. Teleconnections in the geopotential height field during the Northern Hemisphere winter. *Mon. Weather Rev.* **1981**, *109*, 784–812. [[CrossRef](#)]
31. Hong, X.; Lu, R. The meridional displacement of the summer Asian jet, Silk Road pattern, and tropical SST anomalies. *J. Clim.* **2016**, *29*, 3753–3766. [[CrossRef](#)]
32. Zhang, L.; Wu, P.; Zhou, T.; Xiao, C. ENSO transition from La Niña to El Niño drives prolonged spring-summer drought over North China. *J. Clim.* **2018**, *31*, 3509–3523. [[CrossRef](#)]
33. Dai, L.; Wright, J.S.; Fu, R. Moisture and energy budget perspectives on summer drought in North China. *J. Clim.* **2020**, *33*, 10149–10167. [[CrossRef](#)]
34. Peng, Y. Simulated interannual teleconnection between the summer North Atlantic Oscillation and summer precipitation in eastern China during the last millennium. *Geophys. Res. Lett.* **2018**, *45*, 7741–7747. [[CrossRef](#)]
35. Kolstad, E.W.; Screen, J.A. Nonstationary Relationship Between Autumn Arctic Sea Ice and the Winter North Atlantic Oscillation. *Geophys. Res. Lett.* **2019**, *46*, 7583–7591. [[CrossRef](#)]
36. Böhm, C.; Reyers, M.; Schween, J.H.; Crewell, S. Water vapor variability in the Atacama Desert during the 20th century. *Glob. Planet. Chang.* **2020**, *190*, 103192. [[CrossRef](#)]
37. Laloyaux, P.; de Boisseson, E.; Balmaseda, M.; Bidlot, J.R.; Broennimann, S.; Buizza, R.; Dalhgren, P.; Dee, D.; Haimberger, L.; Hersbach, H.; et al. CERA-20C: A coupled reanalysis of the twentieth century. *J. Adv. Model. Earth Syst.* **2018**, *10*, 1172–1195. [[CrossRef](#)]
38. Harris, T.; Osborn, T.J.; Jones, P.; Lister, D. Version 4 of the CRU TS monthly high-resolution gridded multivariate climate dataset. *Sci. Data* **2020**, *7*, 109. [[CrossRef](#)]

39. University of East Anglia Climatic Research Unit; Harris, I.C.; Osborn, T.J.; Jones, P.; Lister, D. CRU TS4.03: Climatic Research Unit (CRU) Time-Series (TS) version 4.03 of high-resolution gridded data of month-by-month variation in climate (Jan. 1901–Dec. 2018). *Cent. Environ. Data Anal.* **2020**. [[CrossRef](#)]
40. Willmott, C.J.; Matsuura, K. Terrestrial Air Temperature and Precipitation: Monthly and Annual Time Series (1950–1999). 2001. Available online: http://climate.geog.udel.edu/~climate/html_pages/README.ghcn_ts2.html (accessed on 5 September 2020).
41. Peng, D.; Zhou, T. Why was the arid and semiarid northwest China getting wetter in the recent decades? *J. Geophys. Res. Atmos.* **2017**, *122*, 9060–9075. [[CrossRef](#)]
42. Mantua, N.J.; Hare, S.R.; Zhang, Y.; Wallace, J.M.; Francis, R.C. A Pacific Interdecadal Climate Oscillation with Impacts on Salmon Production*. *Bull. Am. Meteorol. Soc.* **1997**, *78*, 1069–1080.
43. Kosaka, Y.; Xie, S.P.; Lau, N.C.; Vecchi, G.A. Origin of seasonal predictability for summer climate over the Northwestern Pacific. *Proc. Natl. Acad. Sci. USA* **2013**, *110*, 7574–7579. [[CrossRef](#)]
44. Huang, Y.; Wang, H.; Fan, K.; Gao, Y. The western Pacific subtropical high after the 1970s: Westward or eastward shift? *Clim. Dyn.* **2015**, *44*, 2035–2047. [[CrossRef](#)]
45. Zhang, L.; Zhou, T.; Wu, P.; Chen, X. Potential Predictability of North China Summer Drought. *J. Clim.* **2019**, *32*, 7247–7264.
46. Hersbach, H.; Bell, B.; Berrisford, P.; Hirahara, S.; Horányi, A.; Muñoz-Sabater, J.; Nicolas, J.; Peubey, C.; Radu, R.; Schepers, D.; et al. The ERA5 global reanalysis. *J. R. Meteorol. Soc.* **2020**, *146*, 1999–2049. [[CrossRef](#)]
47. Wei, W.; Zhang, R.; Wen, M.; Rong, X.; Li, T. Impact of Indian summer monsoon on the South Asian High and its influence on summer rainfall over China. *Clim. Dyn.* **2014**, *43*, 1257–1269.
48. Wei, W.; Zhang, R.; Wen, M.; Yang, S. Relationship between the Asian westerly jet stream and summer rainfall over Central Asia and North China: Roles of the Indian Monsoon and the South Asian High. *J. Clim.* **2017**, *30*, 537–552.
49. Zhang, P.; Liu, Y.; He, B. Interannual variation of the South Asian High and its relation with Indian and East Asian summer monsoon rainfall. *J. Clim.* **2016**, *28*, 2623–2634.
50. Tao, L.; Li, T.; Ke, Y.-H.; Zhao, J.-W. Causes of interannual and interdecadal variations of the summertime Pacific–Japan-like pattern over East Asia. *J. Clim.* **2017**, *30*, 8845–8864. [[CrossRef](#)]
51. Cram, T.A.; Compo, G.P.; Yin, X.; Allan, R.J.; McColl, C.; Vose, R.S.; Whitaker, J.S.; Matsui, N.; Ashcroft, L.; Auchmann, R.; et al. The international surface pressure databank version 2. *Geosci. Data J.* **2015**, *2*, 31–46. [[CrossRef](#)]
52. NOAA Physical Sciences Laboratory, ISPD Databank, Locations of Stations in International Surface Pressure Databank Version 3.7. Available online: <https://psl.noaa.gov/data/ISPD> (accessed on 8 December 2020).